PARAMETRIC MODELING OF AC-DC CONVERTERS FOR POWER SYSTEM TRANSIENT STUDIES

by

Parastoo Sadat Hosseinian

B.Sc., Amirkabir University of Technology, 2017

M.Sc., Amirkabir University of Technology, 2019

A THESIS SUBMITTED IN PARTIAL FULFILLMENT OF

THE REQUIREMENTS FOR THE DEGREE OF

MASTER OF APPLIED SCIENCE

in

THE FACULTY OF GRADUATE AND POSTDOCTORAL STUDIES

(Electrical and Computer Engineering)

THE UNIVERSITY OF BRITISH COLUMBIA

(Vancouver)

August 2023

The following individuals certify that they have read, and recommend to the Faculty of Graduate and Postdoctoral Studies for acceptance, the thesis entitled:

Parametric modeling of ac-dc converters for power system transient studies

submitted by   Parastoo Sadat Hosseinian   in partial fulfillment of the requirements for

the degree of   Master of Applied Science

in   Electrical and Computer Engineering

Examining Committee:

Dr. Juri Jatskevich, Professor, Electrical and Computer Engineering, UBC
Supervisor

Dr. Hermann Dommel, Professor Emeriti, Electrical and Computer Engineering, UBC
Supervisory Committee Member

Dr. Christine Chen, Associate Professor, Electrical and Computer Engineering, UBC
Supervisory Committee Member

Abstract

The AC-DC line-commutated converters and voltage-source converters are widely used in various high-power applications. It is imperative to conduct efficient and precise computer simulations for practical and reliable analysis, design, and study of converter-based power systems. However, detailed switching models of such converters offered by many commercial electromagnetic transient (EMT) simulation programs are known to be computationally expensive.

The average-value modelling (AVM) technique has been developed to achieve computationally efficient models of ac-dc converters for system-level studies. The AVMs neglect the switching and capture the averaged dynamics of converters only. This thesis advances the state-of-the-art and develops computationally efficient and accurate models of ac-dc converters for EMTP-type simulation programs. The proposed approach is able to reconstruct the converter waveforms, including all ac harmonics and dc ripples, without switching circuit elements. Two interfacing methods of the proposed model are presented for indirect and direct interfacing in EMTP-type solutions. The proposed modelling approach is demonstrated to have superior computational efficiency and the ability to accommodate larger time steps compared to detailed switching models of line commutated converters (LCCs) and voltage source converters (VSCs) in ac-dc power systems. It is envisioned that the new models will become adopted by many commonly used offline and real-time EMT simulators.

Lay Summary

Development and analysis of power systems containing ac–dc power-electronic converters demand comprehensive computer studies and simulations. Efficient modelling of electrical components such as electrical machines, transmission lines, and power-electronic converters is essential. Nevertheless, models of power-electronic converters have always posed challenges in power systems simulations.

This thesis proposes new models of ac-dc line-commutated and voltage source converters that are computationally more efficient compared to the existing conventional detailed switching models. The proposed models have been validated through computer studies and demonstrated to offer significant computational benefits. It is envisioned that many offline and real-time electromagnetic transient programs and simulators will adopt the proposed models, thus providing helpful tools for researchers and engineers worldwide.

Preface

Most of the research results presented in this thesis have already been published in or will be submitted to scientific journals and conference proceedings. In all of the papers, I was responsible for most of the works, including deriving the mathematical formulations, developing the proposed models, establishing the simulation models, executing simulations, analyzing results, and initiating and editing the drafts. All of these works have been done under the supervision of Dr. Juri Jatskevich, who provided guidance, valuable feedback, and comments throughout every stage and helped in writing and editing the papers. The coauthor, Dr. Seyyedmilad Ebrahimi, also contributed constructive feedback and instructions throughout discussions, debugging simulations, and paper revisions.

The articles resulting from this work are listed below:

Chapter 2 is based on the following conference paper:

P. S. Hosseinian, S. Ebrahimi and J. Jatskevich, "Hybrid parametric average-value/detailed modeling of classic HVDC systems," in *Proc. Int. Conf. Electr. Comp. Eng. Technol. (ICECET)*, Prague, Czech Republic, Jul. 20-22, 2022, pp. 1-6.

Chapter 3 is based on the following conference paper:

P. S. Hosseinian, S. Ebrahimi and J. Jatskevich, "Average-value modeling of hybrid LCC-VSC HVDC systems with direct interfacing in PSCAD/EMTDC," in *Proc.* IEEE *Int. Symp. NFOTEH-JAHORINA (INFOTEH)*, East Sarajevo, Bosnia and Herzegovina, Mar. 15-17, 2023, pp. 1-6.

Chapter 4 is based on the following journal paper:

P. S. Hosseinian, S. Ebrahimi and J. Jatskevich, "Detailed parametric modeling of AC–DC converters for EMT simulators," (to be submitted), pp. 1–10.

Table of Contents

List of Tables

List of Figures

xiii

List of Symbols

In this thesis, scalars are written using italic fonts [e.g., i_a], and vectors are denoted by lowercase bold letters [e.g., $\mathbf{i}_{abc}$], and matrices are denoted by uppercase bold letters [e.g., $\mathbf{R}_{abc}$]. Only basic variables are aggregated in this section; all other variables are defined explicitly throughout the thesis.

α	Firing angle
β	Period of ripples on converter dc and qd variables
δ	Modulation angle
$\mathbf{e}_{abc}$	Source abc voltage
$\mathbf{e}_{h\text{CON}}$	Converter voltage history vector
$\varphi(.)$	Phase shift parametric function
$\mathbf{G}_{\text{CON}}$	Converter conductance matrix
$\mathbf{i}_{abc}$	Converter abc current
i_{comp}	Compensation dc current
i_{dc}	Converter dc current
$\mathbf{I}_{h\text{CON}}$	Converter current history vector
$\mathbf{K}$	Park's transformation matrix
M	Modulation index

$\mathbf{R}_{CON}$	Converter resistance matrix
θ_e	Converter phase *a* angle
θ_{rec}	Reconstruction angle
θ_s	Source phase *a* angle
$\mathbf{v}_{abc}$	Converter *abc* voltage
v_{dc}	Converter dc voltage
$w_i(.)$	Current parametric function
$w_v(.)$	Voltage parametric function
z_d	Dynamic impedance

List of Abbreviations

AAVM — Analytical Average Value Model

ac — Alternative Current

AVM — Average Value Model

dc — Direct Current

DNSM — Detailed Non-Switching Models

DSM — Detailed Switching Models

EMT — Electromagnetic Transients

GPAVM — Generalized Parametric Average Value Model

HPAVM — Hybrid Parametric Average-Value/Detailed Model

HVDC — High Voltage Direct Current

IGBT — Insulated-Gate Bipolar Transistor

LCC — Line-commutated Converter

LCI — Line-commutated Inverter

LCR — Line-commutated Rectifier

PAVM — Parametric Average Value Model

SPWM — Sinusoidal Pulse Width Modulation

VSC — Voltage-Source Converter

Acknowledgements

I would like to express my heartfelt gratitude to my supervisor, Dr. Juri Jatskevich, for his invaluable academic guidance, constructive feedback, and instructions throughout my research journey. His wealth of knowledge and passion taught me effective approaches to learning, researching, and working. I consider myself fortunate and appreciative to have had such an excellent, enthusiastic, and supportive supervisor during my academic pursuits. Additionally, I would thank Dr. Jatskevich for providing funding for my research through the Natural Science and Engineering Research Council (NSERC) under the Collaborative Research and Development (CRD) grant "Research and Development of Advanced Techniques for EMT Simulation of Modern Energy System." I would also like to extend my appreciation to Dr. Seyyedmilad Ebrahimi, whose insightful remarks and constructive input were incredibly helpful to me.

I am also very thankful to my examining committee members, Dr. Hermann Dommel and Dr. Christine Chen, for dedicating their valuable time and providing helpful comments and feedback to improve my thesis. I would also like to extend my thanks to the faculty, staff, and my peers at UBC for their support throughout my studies, which significantly contributed to my progress in this field. Specifically, I am deeply thankful to my colleagues and friends in the UBC Electric Power and Energy Systems research group. I would like to thank Erfan Mostajeran, Arash Safavizadeh, Taleb Vahabzadeh, Jinhe Zhou, Siqi Wu, Gloria Wang, Sheraz Baig, and many others, for their support and inspiring working environment in our lab.

I owe a debt of gratitude to my wonderful parents, Zahra and Hossein, for their unconditional support throughout all years of my life and studies. I also thank my dearest friend, Ehsan, whose encouragement paved the way for me to undertake this remarkable journey.

Dedication

To my lovely Mom and Dad

Chapter 1: Introduction

1.1 Motivation

POWER-ELECTRONIC converters play an important role in modern energy systems by connecting new energy resources to conventional power grids. Two main types of converters are commonly deployed in ac-dc conversion systems: line-commutated converters (LCCs), composed of diode or thyristor switches; and voltage-source converters (VSCs), composed of forced-commutated transistors, e.g., Insulated-Gate Bipolar Transistors (IGBTs) and similar semiconductor devices.

In many applications, the 2-level LCCs and VSCs are used as basic building blocks due to the simplicity and reliability of this technology [1], [2]. Such applications include the classic high voltage direct current (HVDC) transmission systems [3]–[5], power systems of vehicles [6], [7], ships, and aircraft, induction furnaces [8], exciters of synchronous generators [9]–[11], etc.

Among these various applications, HVDC transmission systems are extensively utilized worldwide for bulk, long-distance power delivery due to their high power transmission capacity and high efficiency [3]. The LCC-based HVDC transmission systems are commercially deployed because of their reliable and cost-effective operation [12]. Despite their advantages, the LCC-HVDC systems have some drawbacks, such as commutation failure [13], and the need for strong ac systems and dc voltage polarity reversal in case power flow direction changes [4]. The VSC-based HVDC systems have been utilized increasingly over the recent decades [13]. Unlike the LCC-based HVDC systems, the VSC-based HVDC technology offers the ability of independent regulation for active and reactive power [13]. Also, the on/off states of IGBT switching devices of VSCs are independent of the grid, which makes this technology more suitable for weak systems

1

[4]. However, compared to the LCC-HVDC systems, the VSC-HVDC systems have a smaller power rating, more loss, and a higher installation cost [12]. Utilizing the LCCs and VSCs in a hybrid HVDC system brings the benefits of both technologies. A possible topology is to use the LCCs on the sending end, considering their higher operating efficiency, and the VSCs on the receiving end, due to their more flexible power control [14].

Although the wide adoption of such HVDC systems and, in general, the LCC and VSC ac-dc converters due to their simplicity and reliability, the LCRs and VSCs produce ac harmonics and dc ripples [15], [16], which may affect other components in the power system [17] (e.g., protection systems and relays, harmonic compensation measures, transformers, generators, etc.).

Therefore, accurate modelling and simulation of these converters, including the prediction of entire waveforms of ac and dc variables, are considered extremely important. These models should be able to predict the behaviour of individual components and the entire system ahead of the actual hardware implementation. Hence, offline and real-time electromagnetic transient (EMT) simulations of systems with such converters are often conducted to analyze waveforms of ac and dc terminal variables, design harmonic filters, etc. Commercial time domain simulation programs, including either state-variable-based (SV-based) programs such as MATLAB/Simulink, Simscape Electrical toolbox, PLECS, RT-Lab, and Typhoon HIL, or the nodal-analysis-based electromagnetic transient programs (EMTP-type), such as EMTP-RV, PSCAD/EMTDC, RTDS, and MicroTran, can be employed for transient studies of such ac-dc conversion systems.

For such purposes, the conventional detailed switching models of these ac-dc converters are typically available as standard library components in these commercial EMT simulation programs. These switching models offer accurate solutions by considering the operation of every semiconductor device individually. However, due to many discrete switching events which need

2
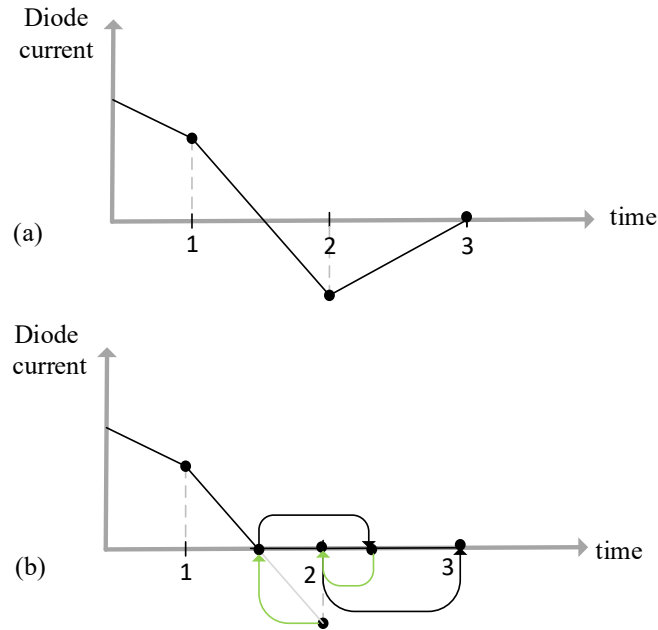
Figure 1.1 Diode current for: (a) non-interpolated switch, and (b) interpolated switch.

to be detected/predicted, these models typically require significant computing resources [18]. Offline programs may apply interpolation and zero-crossing detection, which are numerically costly. For instance, PSCAD/EMTDC employs interpolation to facilitate the precise estimation of switching events within a typical time step of power system simulation [19]. Figure 1.1 (a) and (b) depict the solution procedure for non-interpolated and interpolated switches.

As shown in Figure 1.1 (b), initially, the solution is computed for $t = 1$ when the diode current is positive and the switch is on. Then, for the next time step, at $t = 2$, the solution is computed again. The program will calculate the current zero crossing moment if the new diode current is negative. It would interpolate all voltages and currents to this moment and then switch the diode off. Assuming that there is no further switching at this time step, the main program would appropriately calculate the voltages at the next time step. Afterward, the program interpolates the
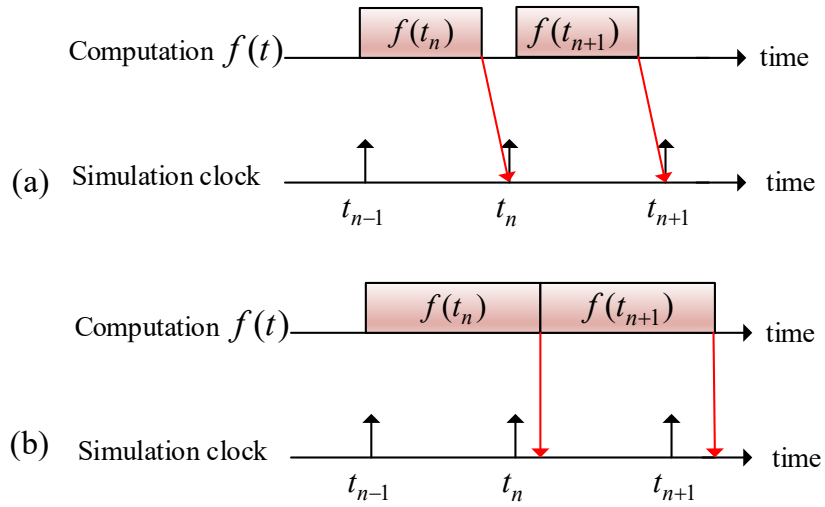
Figure 1.2 Real-time simulation: (a) synchronized, and (b) overrun.

voltage back to $t = 2$ to bring the simulation back on track with integral time steps. The voltages

and currents at $t = 2$ can be computed, and the program continues the normal solution to $t = 3$.

Therefore, two interpolations are required for each switching event. Thus, such detailed

models typically require significant computational resources to handle switching events and

commutations. Due to many discrete switching events, this may result in a long run time in offline

simulations.

At the same time, interpolation may not be practical in real-time simulation [20] due to its

high computational cost. Therefore, real-time EMT simulation programs must use small time-step

to handle the switching events. This may cause time-step overflow (i.e., overrun) in real-time when

the computations in each step exceed the time-step window [21], [22], as shown in Figure 1.2 (b),

compare to the synchronized simulation shown in Figure 1.2 (a), where the computations can fit

in the time-step window.

4

The high computational cost makes the detailed switching models (DSMs) of converters simulation bottlenecks for system-level studies, especially when the power system has many switching components.

To avoid the computational cost of DSMs, efficient alternatives, such as the dynamic phasor models [23]–[26] and average value models (AVMs) [27]–[33], have been developed. These models facilitate the simulation of large-scale power systems by adopting larger time steps at the cost of neglecting the switching details of individual semiconductor devices. In AVMs, the details of switching are neglected, and slower dynamics are considered only. Therefore, AVMs do not require zero-crossing detections and are able to be simulated with larger time steps, making them favourable for system-level studies [34].

1.2 Literature review

The AVMs can be classified as analytical AVMs (AAVMs) [27], [35]–[37] and parametric AVMs (PAVMs) [34], [38], [39] depending on the methodology used to derive the average-value relationships among the variables. In AAVM [27], [35]–[37], the average values of ac and dc variables are defined by analytical formulations. The AAVMs are valid for the specific mode of operation for which the model is derived. Also, losses and non-idealities are neglected in the typical AAVMs. To address these limitations, the PAVMs [34], [38], [39] were developed for LCRs, and have proven accurate under various operating conditions. In PAVMs, algebraic formulations are used to relate the average values of the dc-side and ac-side transformed variables (in qd coordinates) using the so-called parametric functions that are obtained numerically [34].

Several AVMs have been developed specifically for HVDC systems [24], [40]–[43]. In [40], an AVM has been developed for the HVDC system, which is constructed numerically. This

5

method reconstructs only the average values of ac and dc variables. In [24], [42], [43], AVMs are proposed for modelling HVDC systems using dynamic phasors. In [42], Only the fundamental frequency dynamics of the ac variables are reconstructed. The proposed models in [24], [43] are able to retain higher-order harmonic components of ac variables, making them more accurate. However, the complex derivation of the analytical switching functions, which relate the ac and dc variables, can restrict the order of retained harmonics. Also, the validity of the models for different operating points is restricted as the models are analytically derived for a single mode of operation, which can cause significant errors in other modes of operation.

Some methods have been developed to enable the reconstruction of ac harmonic variables. The proposed parametric dynamic phasor model in [23] presents a valid method for different operating modes of LCCs, including 5th and 7th ac harmonics.

A generalized PAVM (GPAVM) was presented in [44] for LCRs. This GPAVM model is able to reconstruct selected harmonics of the ac variables in addition to their fundamental frequency components (by transforming them into multiple *qd* reference frames corresponding to different selected harmonics). Including more harmonics increases the complexity of the GPAVM.

To reduce this complexity, a hybrid PAVM/detailed model (HPAVM) of LCRs was proposed in [45], which uses only one *qd* transformation. This was done using extra parametric functions for the oscillatory components for reconstructing ac harmonics and dc ripples as accurately as the DSMs. However, in the HPAVM, the harmonics of the ac variables and the ripples of the dc variables are computed separately from their fundamental frequency components and averages, respectively, which comes with an additional computational cost.

The AVMs, PAVMs, GPAVM, and HPAVM are typically interfaced with the external networks using controlled voltage/current sources [33], [34], [38], [39], [44], [45]. Some state-

6

variable-based programs [46] can solve the external network simultaneously with the AVMs. However, in EMTP-type programs with non-iterative solutions (e.g., PSCAD and RSCAD), one time-step delay is needed between the solution of the external network and the AVM interfacing variables [47] (referred to as indirect interfacing). This delay may cause numerical inaccuracy or instability at large simulation time steps.

To avoid the time step delay, in [48], the AAVM formulations for three-phase LCR are discretized using the trapezoidal integration rule and interfaced directly with the external network circuit. However, the model is limited to a specific operating mode as the general restriction of the analytical approach.

Direct interfacing techniques have been developed in [47] and [49] for AVMs of LCRs and VSCs in the nodal analysis-based solution, eliminating the interfacing time step delay. This was done by linearizing the average-value relations and formulating a conductance matrix for the LCR PAVM and VSC AVM to be solved as part of the overall network solution. However, the directly-interfaced methods are based on the classic AVM of the converters, and are only able to preserve the fundamental frequency components of the ac waveforms and the average values of the dc variables.

1.3   Research Objectives

Considering the rapid growth of computer studies in the power systems industry, preserving computational resources is a significant priority. This also includes optimizing the utilization of essential CPU cores in real-time simulators, a goal that the proposed model aims to achieve. The primary purpose of this thesis is to develop new models of ac-dc converters that consider all the details of system variables (i.e., harmonics and ripples) similar to switching

7

detailed models, while enabling simulation with larger time-steps without significant loss of numerical accuracy. This leads to reduced computational cost and efficient simulations, thereby facilitating the studies of power systems that include many ac-dc converters.

1.3.1 Objective I: Extend the hybrid parametric average-value/detailed modelling to the line-commutated inverters

Recently, the so-called hybrid parametric average-value/detailed (HPAVM) model was developed for line-commutated rectifiers (LCRs) [45], which proposed a new method to construct the entire ac and dc waveforms consistent with the switching models (i.e., considering all harmonics for ac variables along with ripples on dc variables). This thesis's first objective is to extend the HPAVM formulation to line-commutated inverters (LCI). Specifically, dynamic admittance and new parametric functions are derived based on [45] for average values and harmonics/ripples of LCI. The objective achieves a numerically efficient model that outperforms the conventional switching models by allowing larger time steps for simulations. The HPAVM also provides the flexibility of choosing either to contain the ac-side harmonics and/or dc-side ripples or to ignore them.

1.3.2 Objective II: Develop the directly-interfaced AVMs of LCRs in PSCAD

So far, the directly-interfaced AVMs (DI-AVMs) of LCCs [47] and VSCs [49] have been developed for nodal analysis-based solutions. In [47] and [49], DI-AVMs have been demonstrated using EMTP-solution in MATLAB. This objective aims to implement the user-defined component (Component Wizard) of the DI-AVMs of LCRs in PSCAD/EMTDC to directly interface with ac and dc subsystems similar to the PSCAD built-in electrical components.

8

1.3.3 Objective III: Develop detailed parametric modelling of ac-dc converters for EMT simulators

This objective focuses on extending the research carried out in the previous two objectives. The main goal is to develop a detailed and efficient modelling approach for ac-dc converters, including LCRs and VSCs. The proposed methodology is based on parametric functions that relate ac and dc variables in the instantaneous sense. This allows the reconstruction of the waveforms of voltages and currents without topological changes in the converter circuit. Furthermore, indirect and direct interfacing methods are presented for the proposed detailed non-switching model of converters. In addition, the model offers an accurate solution for different load compositions in the dc network in contrast to the prior methods, where the accuracy of ripples and harmonics are compromised by the network employed to establish parametric functions.

1.4 Platforms for Verifications

This thesis uses various simulation software programs to conduct steady-state and transient studies and verify the proposed models against the existing models, as needed in each case. The considered programs include MATLAB/Simulink [50], Simscape Electrical (SimPowerSystems) toolbox [51], PSCAD/EMTDC [52], and RSCAD [53] using NovaCor of RTDS for real-time simulations. These programs have gained general acceptance among engineers and researchers in industry and academia and are known for their ability to accurately simulate power systems, including power-electronic-based converters. Hence, the detailed models provided by these programs can be used as appropriate benchmarks for evaluating the proposed models introduced in this thesis. Furthermore, to ensure consistency, the simulation studies are carried out within the

same simulation and computational environment when comparing the numerical and computational efficiency of the respective models.

Chapter 2: Hybrid Parametric Average-Value/Detailed Modeling of Classic HVDC Systems

Classic high voltage direct current (HVDC) transmission systems based on line-commutated converters (LCCs) offer reliable technologies widely used for long-distance transmission across power grids. LCC-based HVDC systems have played a vital role in overcoming conventional AC transmission limitations by enabling efficient, low-loss power transmission over vast distances [3]. Asynchronous grids operating at different frequencies or phases can also be interconnected using LCC-based HVDC systems. This capability allows power to be transferred smoothly between grids, enhancing grid reliability and stability. The LCC-based HVDC system consists of two converter stations: the line-communicated rectifier (LCR) station at the sending end and the line-communicated inverter (LCI) station at the receiving end.

This chapter first extends the formulation of the HPAVM [45] to LCIs. Thereafter, the proposed HPAVM of LCIs and the HPAVM of LCRs are used to model a classic LCC-based HVDC system. The numerical performance of the proposed hybrid parametric average-value/detailed modelling technique is investigated on a classic line-commutated-based HVDC system. It is verified that the proposed HPAVM can be superior compared to switching models of HVDC systems by allowing simulations with large time steps while maintaining acceptable accuracy.

2.1   Continuous Hybrid PAVM of HVDC Systems

A generic LCC-based classic HVDC system is studied herein, as shown in Figure 2.1. Therein, the two ac subsystems are interconnected by two six-pulse LCCs through a dc subsystem.
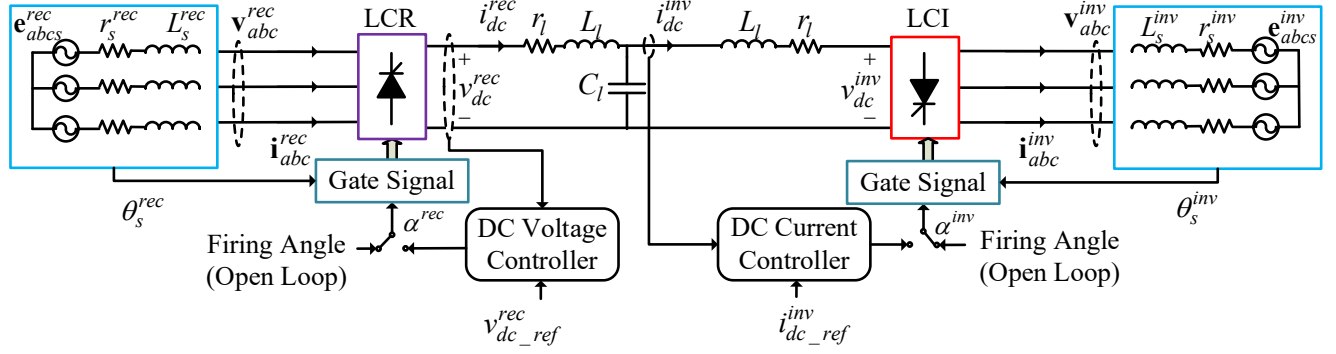
Figure 2.1 Generic LCC-based classic HVDC system containing a six-pulse LCR and an LCI.

Throughout this chapter, the superscripts "rec" and "inv" are used to refer to the rectifier and inverter sides, respectively. The dc subsystem consists of the HVDC transmission line represented by a T-model [54] with line resistance r_l, inductance L_l, and capacitance C_l. The LCR and LCI are both composed of thyristor switches with on-state resistance R_{on} and voltage drop V_{on}, which determines the conduction losses. The ac-side subsystems may be represented by their Thévenin equivalents [55] consisting of sources and impedances. The Thévenin impedances are modeled by resistances r_s^{rec} and r_s^{inv}, and inductances L_s^{rec} and L_s^{inv}. The three-phase equivalent sources $\mathbf{e}_{abcs}^{rec}$ and $\mathbf{e}_{abcs}^{inv}$ are considered to be sinusoidal. Also, the angles of their phase a are denoted by θ_s^{rec} (for rectifier-side) and θ_s^{inv} (for inverter-side) in Figure 2.1. The angle of the rectifier and inverter ac terminal voltages $\mathbf{v}_{abc}^{rec}$ and $\mathbf{v}_{abc}^{inv}$ can be defined as [45] (with the fundamental component of their phase a as the reference)

$$\theta_e^{rec} = \int \omega_e^{rec} dt, \quad \omega_e^{rec} = 2\pi f_e^{rec}, \tag{2.1}$$

$$\theta_e^{inv} = \int \omega_e^{inv} dt, \quad \omega_e^{inv} = 2\pi f_e^{inv}, \tag{2.2}$$

12

where ω_e^{rec} (f_e^{rec}) and ω_e^{inv} (f_e^{inv}) are the frequency of rectifier- and inverter-side ac subsystems in rad/s (Hz), respectively.

The rectifier and inverter side ac voltages $\mathbf{v}_{abc}^{rec}$ and $\mathbf{v}_{abc}^{inv}$, and currents $\mathbf{i}_{abc}^{rec}$ and $\mathbf{i}_{abc}^{inv}$ can be expressed by their fundamental and harmonic components as

$$\mathbf{v}_{abc}^{rec} = \mathbf{v}_{abc}^{1,rec} + \sum_n \mathbf{v}_{abc}^{n,rec}, \quad \mathbf{i}_{abc}^{rec} = \mathbf{i}_{abc}^{1,rec} + \sum_n \mathbf{i}_{abc}^{n,rec}, \tag{2.3}$$

$$\mathbf{v}_{abc}^{inv} = \mathbf{v}_{abc}^{1,inv} + \sum_n \mathbf{v}_{abc}^{n,inv}, \quad \mathbf{i}_{abc}^{inv} = \mathbf{i}_{abc}^{1,inv} + \sum_n \mathbf{i}_{abc}^{n,inv}, \tag{2.4}$$

where n denotes the order of harmonics; here equal to $\{5, 7, 11, 13...\}$.

To establish the HPAVM formulation, the ac variables are transformed to qd reference frames rotating with θ_e^{rec} and θ_e^{inv} using the Park transformation defined in Appendix A as

$$\mathbf{v}_{qd}^{e,rec} = \mathbf{K}\left(\theta_e^{rec}\right)\mathbf{v}_{abc}^{rec}, \quad \mathbf{i}_{qd}^{e,rec} = \mathbf{K}\left(\theta_e^{rec}\right)\mathbf{i}_{abc}^{rec}, \tag{2.5}$$

$$\mathbf{v}_{qd}^{e,inv} = \mathbf{K}\left(\theta_e^{inv}\right)\mathbf{v}_{abc}^{inv}, \quad \mathbf{i}_{qd}^{e,inv} = \mathbf{K}\left(\theta_e^{inv}\right)\mathbf{i}_{abc}^{inv}, \tag{2.6}$$

where $\mathbf{K}$ is Park's transformation matrix. Here, $\mathbf{v}_{qd}^{e,rec} / \mathbf{i}_{qd}^{e,rec}$ and $\mathbf{v}_{qd}^{e,inv} / \mathbf{i}_{qd}^{e,inv}$ are the rectifier- and inverter-side transformed voltages/currents, respectively. These transformed qd variables consist of average values and oscillatory components, which can be expressed as

$$\mathbf{v}_{qd}^{e,rec} = \overline{\mathbf{v}}_{qd}^{e,rec} + \tilde{\mathbf{v}}_{qd}^{e,rec}, \quad \mathbf{i}_{qd}^{e,rec} = \overline{\mathbf{i}}_{qd}^{e,rec} + \tilde{\mathbf{i}}_{qd}^{e,rec}, \tag{2.7}$$

$$\mathbf{v}_{qd}^{e,inv} = \overline{\mathbf{v}}_{qd}^{e,inv} + \tilde{\mathbf{v}}_{qd}^{e,inv}, \quad \mathbf{i}_{qd}^{e,inv} = \overline{\mathbf{i}}_{qd}^{e,inv} + \tilde{\mathbf{i}}_{qd}^{e,inv}, \tag{2.8}$$

where the variables with bar – represent the average values and the variables with ~ represent the oscillatory components. It is noted that the oscillatory components of ac variables in qd coordinates correspond to the sum of the ac harmonics in abc coordinates.

As well as the ac-side variables, the dc-side variables can be decomposed into the average and oscillatory components as

$$v_{dc}^{rec} = \bar{v}_{dc}^{rec} + \tilde{v}_{dc}^{rec}, \quad i_{dc}^{rec} = \bar{i}_{dc}^{rec} + \tilde{i}_{dc}^{rec}, \tag{2.9}$$

$$v_{dc}^{inv} = \bar{v}_{dc}^{inv} + \tilde{v}_{dc}^{inv}, \quad i_{dc}^{inv} = \bar{i}_{dc}^{inv} + \tilde{i}_{dc}^{inv}, \tag{2.10}$$

using similar symbols for components (i.e., – for the average values and ~ for the oscillatory components).

For six-pulse converters considered in this paper, the periods of the ripples on qd ac variables and the dc variables can be expressed as [45]

$$\beta = \pi / 3, \quad T^{rec} = \beta / \omega_e^{rec}, \quad T^{inv} = \beta / \omega_e^{inv}, \tag{2.11}$$

where β is the period of ripples in radians, and T^{rec} and T^{inv} are its corresponding values in seconds for the rectifier and inverter, respectively.

After decomposing the transformed ac and dc variables into the average and oscillatory components, these components are obtained by applying a fast averaging to (2.7)–(2.10). Afterward, the so-called parametric functions are presented to establish the relation between the components of the dc- and ac-side variables of both converters.

2.1.1   Formulation of the HPAVM for the Rectifier

In the HPAVM method, the average values of the dc and qd ac variables are related to each other through parametric functions defined as [34]

$$w_v^{1,rec}\left(.\right) = \frac{\left\|\bar{\mathbf{v}}_{qd}^{e,rec}\right\|}{\bar{v}_{dc}^{rec}}, \quad w_i^{1,rec}\left(.\right) = \frac{\bar{i}_{dc}^{rec}}{\left\|\bar{\mathbf{i}}_{qd}^{e,rec}\right\|}. \tag{2.12}$$

14

Also, a parametric function describing the relationship between the angles of fundamental components of the rectifier qd voltages and currents is stored as [34]

$$\varphi^{rec}\left(.\right) = \tan^{-1}\left(\frac{\bar{v}_d^{e,rec}}{\bar{v}_q^{e,rec}}\right) - \tan^{-1}\left(\frac{\bar{i}_d^{e,rec}}{\bar{i}_q^{e,rec}}\right). \tag{2.13}$$

These parametric functions are stored in two-dimensional look-up tables (for various loading conditions) with respect to the rectifier firing angle α^{rec} and the so-called dynamic impedance z_d^{rec}, which determines the loading condition of the rectifier and is defined as [34]

$$z_d^{rec} = \frac{\bar{v}_{dc}^{rec}}{\left\|\bar{i}_{qd}^{e,rec}\right\|}. \tag{2.14}$$

Due to the periodic behaviour of oscillatory components over β, parametric functions are employed to relate them to the average components of the variables. For this purpose, the so-called reconstruction angle is defined for the rectifier as [45]

$$\gamma^{rec} = mod\left(\theta_e^{rec}, \beta\right), \tag{2.15}$$

which is the remainder of the division of θ_e^{rec} by β. Using this angle as an additional dimension for the look-up tables, the oscillatory component of the qd ac-side variables are related to the average values of the rectifier dc-side variables using the parametric functions defined as [45]

$$w_v^{q,rec}\left(.\right) = \frac{\tilde{v}_q^{e,rec}}{\bar{v}_{dc}^{rec}}, \quad w_v^{d,rec}\left(.\right) = \frac{\tilde{v}_d^{e,rec}}{\bar{v}_{dc}^{rec}}. \tag{2.16}$$

Similarly, using γ^{rec}, the ripples on the rectifier dc-side variables can be related to the fundamental components of the rectifier ac-side variable by means of a parametric function described as [45]

15

$$w_i^{dc,rec}(.) = \frac{\tilde{i}_{dc}^{rec}}{\left\| \bar{\mathbf{i}}_{qd}^{e,rec} \right\|}. \tag{2.17}$$

2.1.2 Formulation of the HPAVM for the Inverter

Here, the formulation of the HPAVM [45] is extended to the line-commutated inverters for application in HVDC systems. To this end, the average values of dc and qd ac variables are related to each other using parametric functions defined as

$$w_v^{1,inv}(.) = \frac{\bar{v}_{dc}^{inv}}{\left\| \bar{\mathbf{v}}_{qd}^{e,inv} \right\|}, \quad w_i^{1,inv}(.) = \frac{\left\| \bar{\mathbf{i}}_{qd}^{e,inv} \right\|}{\bar{i}_{dc}^{inv}}. \tag{2.18}$$

Similar to (2.13), a parametric function is used to relate the phase angle of ac voltages/currents for the inverter as

$$\varphi^{inv}(.) = \tan^{-1}\left(\frac{\bar{v}_d^{e,inv}}{\bar{v}_q^{e,inv}}\right) - \tan^{-1}\left(\frac{\bar{i}_d^{e,inv}}{\bar{i}_q^{e,inv}}\right). \tag{2.19}$$

Here, these parametric functions are determined with regard to the inverter firing angle α^{inv} and the dynamic admittance y_d^{inv}, which is representative of the loading condition of the inverter, defined as

$$y_d^{inv} = \frac{\bar{i}_{dc}^{inv}}{\left\| \bar{v}_{qd}^{e,inv} \right\|}. \tag{2.20}$$

The oscillatory components of the inverter variables are captured over β with respect to a reconstruction angle defined as

$$\gamma^{inv} = mod\left(\theta_e^{inv}, \beta\right). \tag{2.21}$$

16

For this purpose, using the oscillatory components on *qd* ac variable (or dc oscillatory components) for the inverter to the average values of dc-side variables (or the fundamental components of ac-side variables), the parametric functions are defined as (with γ^{inv} as an additional argument)

$$w_i^{q,inv}\left(.\right)=\frac{\tilde{i}_q^{e,inv}}{\overline{i}_{dc}^{inv}}, \quad w_i^{d,inv}\left(.\right)=\frac{\tilde{i}_d^{e,inv}}{\overline{i}_{dc}^{inv}}, \tag{2.22}$$

$$w_v^{dc,inv}\left(.\right)=\frac{\tilde{v}_{dc}^{inv}}{\left\|\overline{\mathbf{v}}_{qd}^{e,inv}\right\|}. \tag{2.23}$$

In general, it is not feasible to analytically drive the parametric functions (2.12)–(2.23) under various operating conditions. A numerical method has been established in [45] to obtain the parametric functions from several simulations of the system using switching models of the converters. For this purpose, the subsystem connected to the dc-side of each converter is replaced with a dc current/voltage source or a dc load. Afterward, the loading condition of the converter varies by changing the dc source/load value along with the firing angle of the converter. Then, the parametric functions are computed for each operating point and saved in appropriate lookup tables.

2.1.3   Implementation of the HPAVM of the HVDC System

For the implementation of the HVDC system using the proposed HPAVMs for the LCRs and LCIs, both switching converters are replaced by controlled voltage and current sources, as depicted in Figure 2.2. The inputs to the rectifier HPAVM are the rectifier firing angle α^{rec}, the phase *a* angle of equivalent sources in ac subsystems θ_s^{rec}, rectifier ac current $\mathbf{i}_{abc}^{rec}$ and dc voltage $\overline{v}_{dc}^{rec}$; and its outputs are the rectifier ac voltage $\mathbf{v}_{abc}^{rec}$ and dc current i_{dc}^{rec}, which are used as inputs to the continuous dependent sources interfaced with the ac- and dc- subsystems.
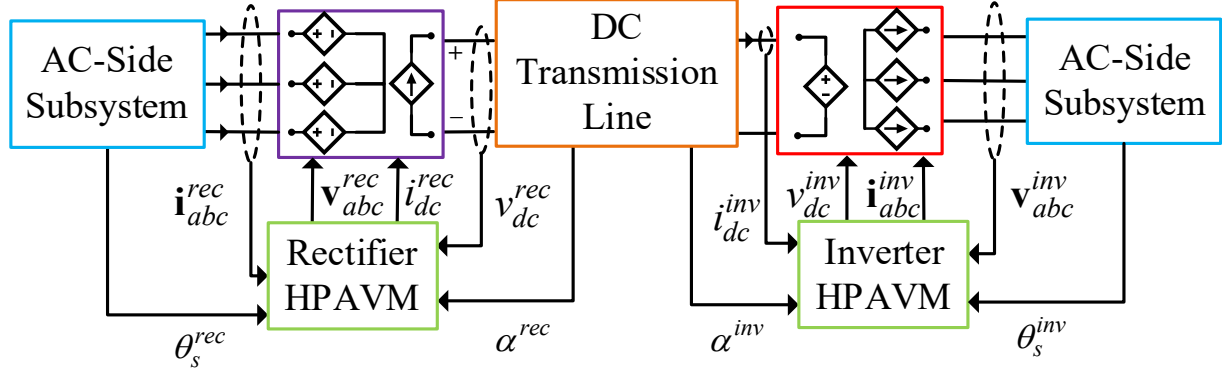
Figure 2.2 Implementation of the LCC-based HVDC system using the proposed HPAVMs of LCRs and LCIs in their interfacing with the ac- and dc-side subsystems via controlled sources.

The inputs to inverter HPAVM are the inverter firing angle α^{inv}, the phase a angle of equivalent sources θ_s^{inv}, inverter ac voltage $\mathbf{v}_{abc}^{inv}$, and dc current i_{dc}^{inv}; and its outputs are the inverter ac current $\mathbf{i}_{abc}^{inv}$ and dc voltage v_{dc}^{inv} to interface with its ac- and dc- subsystems.

The dynamic impedance (for rectifier) and dynamic admittance (for inverter) are calculated based on (2.14) and (2.20), respectively, using the inputs to the HPAVM blocks. Then, the parametric functions are computed based on (2.12), (2.13), (2.16)– (2.19), (2.22), (2.23). Thereafter, using the inputs and the computed parametric functions, the fundamental components of the rectifier ac voltages in qd coordinates are determined as [45]

$$\overline{v}_q^{e,rec} = w_v^{1,rec}(.)\,\overline{v}_{dc}^{rec}\cos(\theta_v^{rec}), \tag{2.24}$$

$$\overline{v}_d^{e,rec} = w_v^{1,rec}(.)\,\overline{v}_{dc}^{rec}\sin(\theta_v^{rec}), \tag{2.25}$$

where θ_v^{rec} represents the angle of the vector $\overline{\mathbf{v}}_{qd}^{e,rec}$ and is calculated as

$$\theta_v^{rec} = \varphi^{rec}(.)+\tan^{-1}\left(\frac{\overline{i}_d^{e,rec}}{\overline{i}_q^{e,rec}}\right). \tag{2.26}$$

18

The oscillatory component of the rectifier qd voltages are also calculated as [45]

$$\tilde{v}_q^{e,rec} = w_v^{q,rec}(.)\bar{v}_{dc}^{rec}, \quad \tilde{v}_d^{e,rec} = w_v^{d,rec}(.)\bar{v}_{dc}^{rec}. \tag{2.27}$$

Finally, the total qd voltages for the rectifier are computed as

$$v_q^{e,rec} = \bar{v}_q^{e,rec} + \tilde{v}_q^{e,rec}, \quad v_d^{e,rec} = \bar{v}_d^{e,rec} + \tilde{v}_d^{e,rec}. \tag{2.28}$$

To interface the voltage source with the ac subsystem, the inverse of Park transformation is used to transform the computed qd voltages back to abc coordinates as

$$\mathbf{v}_{abc}^{rec} = \left[\mathbf{K}(\theta_e^{rec})\right]^{-1}\mathbf{v}_{qd}^{e,rec}. \tag{2.29}$$

The average value of the rectifier-side dc is calculated as

$$\bar{i}_{dc}^{rec} = w_i^{1,rec}(.)\left\|\bar{\mathbf{i}}_{qd}^{e,rec}\right\|, \quad \tilde{i}_{dc}^{rec} = w_i^{dc,rec}(.)\left\|\bar{\mathbf{i}}_{qd}^{e,rec}\right\|. \tag{2.30}$$

The total interfacing dc current can be obtained as

$$i_{dc}^{rec} = \bar{i}_{dc}^{rec} + \tilde{i}_{dc}^{rec}. \tag{2.31}$$

Similarly, using parametric functions and inputs to the inverter HPAVM block, the average values of the inverter ac currents in qd reference frame are computed as

$$\bar{i}_q^{e,inv} = w_i^{1,inv}(.)\bar{i}_{dc}^{inv}\cos(\theta_i^{inv}), \tag{2.32}$$

$$\bar{i}_d^{e,inv} = w_i^{1,inv}(.)\bar{i}_{dc}^{inv}\sin(\theta_i^{inv}). \tag{2.33}$$

Here, θ_i^{inv} represents the angle of the vector $\bar{\mathbf{i}}_{qd}^{e,inv}$ and is calculated as

$$\theta_i^{inv} = \tan^{-1}\left(\frac{\bar{v}_d^{e,inv}}{\bar{v}_q^{e,inv}}\right) - \varphi^{inv}(.). \tag{2.34}$$

The oscillatory components of the qd ac currents of the inverter are also computed as

$$\tilde{i}_q^{e,inv} = w_i^{q,inv}(.)\overline{i}_{dc}^{inv}, \quad \tilde{i}_d^{e,inv} = w_i^{d,inv}(.)\overline{i}_{dc}^{inv}. \tag{2.35}$$

Using fundamental and oscillatory components, the total values of qd currents for the inverter are calculated as

$$i_q^{e,inv} = \overline{i}_q^{e,inv} + \tilde{i}_q^{e,inv}, \quad i_d^{e,inv} = \overline{i}_d^{e,inv} + \tilde{i}_d^{e,inv}. \tag{2.36}$$

To interface the inverter HPAVM current sources with the ac subsystem, the qd currents in (2.36) are transformed back to abc coordinates as

$$\mathbf{i}_{abc}^{inv} = \left[\mathbf{K}\left(\theta_e^{inv}\right)\right]^{-1} \mathbf{i}_{qd}^{e,inv}. \tag{2.37}$$

In addition, the average value and oscillatory component of the controlled dc voltage source of the inverter HPAVM are calculated as

$$\overline{v}_{dc}^{inv} = w_v^{1,inv}(.)\left\|\overline{\mathbf{v}}_{qd}^{e,inv}\right\|, \quad \tilde{v}_{dc}^{inv} = w_v^{dc,inv}(.)\left\|\overline{\mathbf{v}}_{qd}^{e,inv}\right\|. \tag{2.38}$$

Finally, the total interfacing dc voltage is computed as

$$v_{dc}^{inv} = \overline{v}_{dc}^{inv} + \tilde{v}_{dc}^{inv}. \tag{2.39}$$

It is to be noted that one can set the parametric functions $w_i^{dc,rec}$ (2.17) and/or $w_v^{dc,inv}$ (2.23) to zero and obtain only average values for the dc-side variables of the rectifier and/or inverter. Additionally, the parametric functions $w_v^{q,rec}$, $w_v^{d,rec}$ (2.16) and/or $w_i^{q,inv}$, $w_i^{d,inv}$ (2.22) can be set to zero to neglect the ac-side harmonics and obtain only the fundamental components of ac variables for rectifier- and inverter-side ac subsystems, respectively.

2.2 Performance Verification

To evaluate the accuracy and numerical performance of the presented HPAVMs of LCRs and LCIs, the generic LCC-based classic HVDC system of Figure 2.1 is considered for the study.

The parameters of the system are summarized in Appendix B . For comparison, the conventional detailed switching model of the case study system has been implemented in MATLAB/Simulink (as the reference model) using the standard library components of the Simscape toolbox. Furthermore, the HVDC system is implemented in Simulink using the HPAVMs of the rectifier and inverter as described in Section 2.1. Also, to prevent the numerical differentiation in model implementation, low-pass filters are used to calculate voltage drop on L_l of the rectifier side, and L_s^{inv}. Two cases are considered for the HPAVM model: when the ripples on the dc-side variables are reconstructed (denoted by DC Detailed); and when the dc-side ripples are neglected via setting $w_i^{dc,rec}$ and $w_v^{dc,inv}$ equal to zero (denoted by DC AVM).

2.2.1 Numerical Accuracy

Here, it is considered that the system of Figure 2.1 is initially operating in steady-state with the rectifier firing angle α^{rec} set to 40 degrees and the inverter firing angle α^{inv} set to 137 degrees. This results in 370 kV and 348 kV as the average values of the rectifier dc voltage $\bar{v}_{dc}^{rec}$ and inverter dc voltage $\bar{v}_{dc}^{inv}$, respectively, where 1600 MW is transmitted from the rectifier side to the inverter side. It is assumed that the transmitted power is to be decreased to 930 MW while maintaining the rectifier dc voltage at its initial value (i.e., 370 kV). This causes an increase of the inverter dc voltage to 357 kV. For this purpose, at t=0.4 s, the rectifier and inverter firing angles are changed to 42.5 and 139 degrees, respectively.
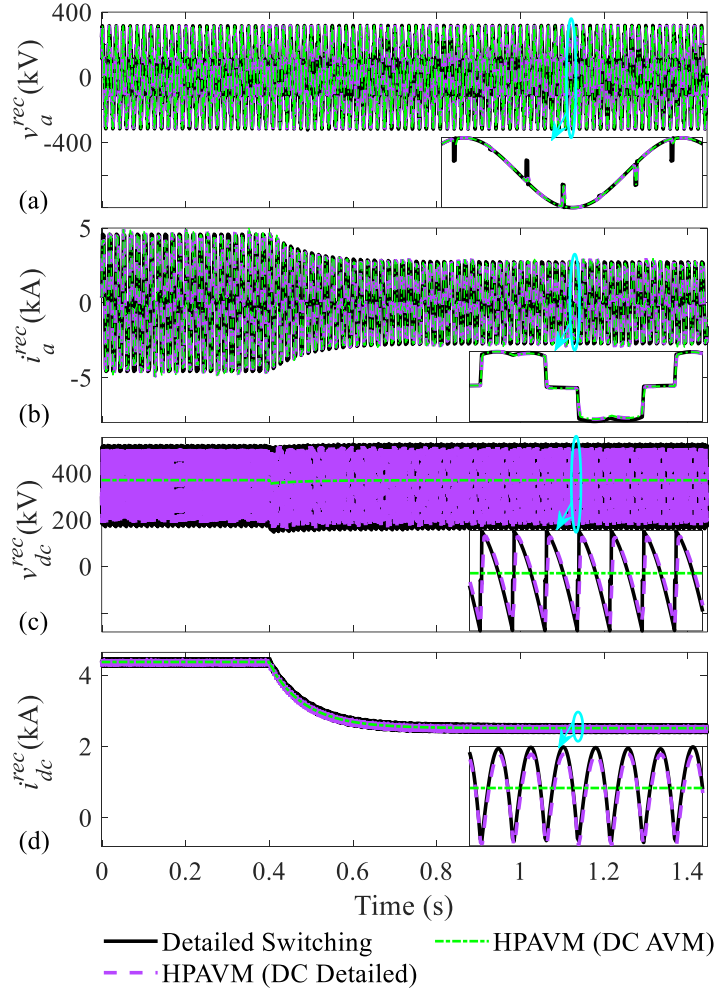
Figure 2.3 Transient response of ac- and dc-side variables of the rectifier-side of HVDC system as obtained by the detailed switching model with time-step of 10 μs and HPAVM with time-step of 150 μs when the transmitted power changed steps from 1600W to 930W at _t_=0.4 s for: (a) rectifier phase a voltage, (b) rectifier phase a current, (c) rectifier dc voltage, and (d) rectifier dc current.

The transient response of dc- and ac- side variables for the rectifier and inverter are presented in Figure 2.3 and Figure 2.4, respectively, as obtained by the detailed switching model with a simulation time-step of 10 _μs_ and the proposed HPAVM with 150 _μs_. As it can be noted from Figure 2.3 (a)-(b) and Figure 2.4 (a)–(b), the proposed HPAVM is able to accurately

22
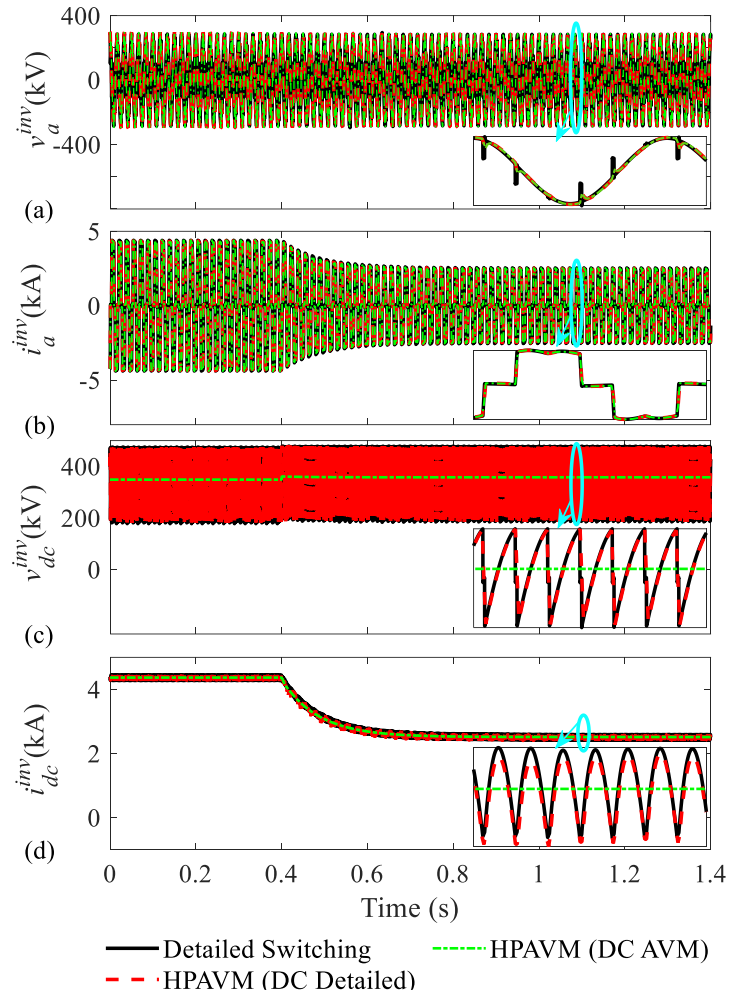
Figure 2.4 Transient response of ac- and dc-side variables of the inverter-side of the HVDC system as obtained by the detailed switching model with time-step of 10 μs and HPAVM with time-step of 150 μs when the transmitted power changed steps from 1600W to 930Wat *t*=0.4 s for: (a) inverter phase a voltage, (b) inverter phase a current, (c) inverter dc voltage (d) inverter dc current.

reconstruct the ac waveforms, including their harmonics during steady-state and transients consistent with the reference detailed switching model.

Also, as it is shown in Figure 2.3 (c)-(d) and Figure 2.4 (c)–(d), the proposed HPAVM (DC Detailed) is capable of reconstructing the dc-side variables of the converter, including their ripples

23

similar to the switching model. Furthermore, the HPAVM (DC AVM) accurately calculates the average values of the dc-side variables. It should also be noted that the HPAVM has allowed a large time-step ($150\mu s$) without numerical inaccuracy/instability as opposed to the switching model, which requires a small time-step (here $10\mu s$) to ensure a valid solution.

2.2.2   Computational Performance

Here, the computational performance of the presented HPAVM is benchmarked against the detailed switching model of the HVDC system. For this purpose, the transient study shown in Section 2.2.1Numerical Accuracy is conducted using the subject models of the HVDC system, where the simulations are continued for 10 seconds. For consistency, all the simulations are run on a PC with Intel Core i7 10750H CPU@2.60GHz, 64-bit, 16GB RAM using the MATLAB/Simulink and fixed-step solver of *ode*3 (i.e., Runge-Kutta 3$^{\text{rd}}$ order). For a fair comparison, the maximum possible time-step that results in acceptable accuracy is considered for each model (i.e., 10 μs for the discrete switching model and 150 μs for the continuous HPAVM). The computational performance of the subject models is summarized in Table 2.1.

As seen in Table 2.1, the HVDC system can be simulated nine times faster using the proposed HPAVM of the converters in comparison with the switching detailed model (i.e., 10.85 s vs. 97.7 s of CPU time), while providing consistent results as verified in Figure 2.3 And Figure 2.4. This is due to the fact that the proposed HPAVM allows a much larger time step (150 μs) as opposed to the switching model, which requires a small time step (10 μs) for accurate zero-crossing detection.

24

Table 2.1 Computational performance of the detailed switching and HPAVM of the HVDC System for the 10-Second transient study

Model	Time-step size	Number of steps	CPU Time
Detailed Switching	10 μs	1,000,000	97.7 s
HPAVM (AC Detailed, DC Detailed)	150 μs	666,666	10.85 s
HPAVM (AC Detailed, DC AVM)	150 μs	666,666	9.27 s

Also, the HPAVM can be slightly more efficient when the dc-side ripples are neglected (i.e., HPAVM – DC AVM with 9.27s) compared to the case that they are reconstrued similarly to the switching model (i.e., HPAVM – DC detailed with 10.85 s).

Chapter 3: Average-Value Modeling of Hybrid LCC-VSC HVDC Systems with Direct Interfacing in PSCAD/EMTDC

As discussed in the previous chapter, HVDC transmission systems are extensively utilized worldwide for long-distance power delivery [3]. In addition to the line-commutated converter (LCC)-based HVDC systems, recently, voltage-source converter (VSC)-based HVDC systems have been increasingly deployed due to their numerous advantages.

In the conventional so-called indirectly-interfaced AVMs (IDI-AVMs) of LCCs and VSCs, the switching converters are substituted with controlled current and voltage sources to interface with the dc and ac networks. With a non-iterative solution, e.g., in PSCAD, a one-time-step delay is required at the interface for the inputs of the AVMs. In simulations with large time steps, this interfacing delay can cause numerical inaccuracy and/or instability of the solution. To address this drawback of IDI-AVMs, the so-called directly-interfaced AVMs (DI-AVMs) of LCCs and VSCs were developed for nodal analysis-based solutions. In the direct interfacing technique, the AVMs of LCCs and VSCs are formulated in the nodal form, and their resultant matrices are solved simultaneously with the external network nodal equations. This eliminates the one-time-step interfacing delay and increases the accuracy at larger time steps.

This chapter investigates the numerical performance of the DI-AVMs of LCCs and VSCs on a hybrid LCC-VSC HVDC system. It is demonstrated that the hybrid LCC-VSC HVDC systems can be simulated with much larger time-steps using DI-AVMs of the converters, and the results are more accurate compared to using the conventional IDI-AVMs.
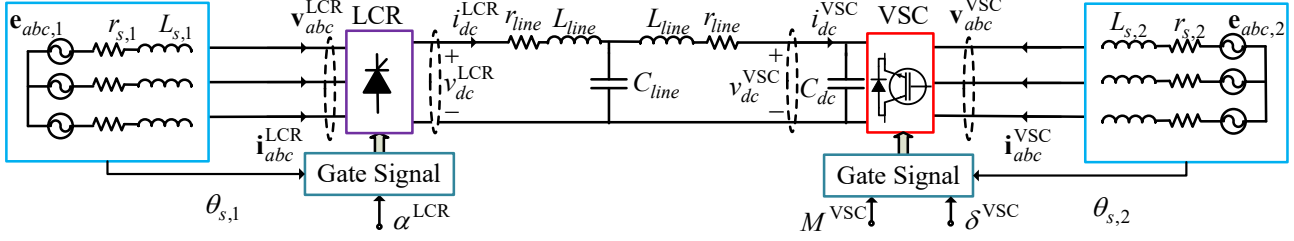
Figure 3.1 A hybrid LCC-VSC HVDC system containing an LCR on sending end and a VSC on receiving end.

3.1 Average-Value Modeling of Hybrid LCC-VSC HVDC System

This Section considers a hybrid LCC-VSC HVDC system, as shown in Figure 3.1. Therein, a line-commutated rectifier (LCR) composed of thyristor switches is utilized to transfer power from the sending end (i.e., left-side) ac subsystem through the dc transmission line. The receiving end (i.e., right-side) ac subsystem is connected to a VSC, which operates in the inverter mode. The capacitance C_{dc} is used to smoothen the dc terminal voltage of VSC. The dc transmission line is demonstrated by a T-model with line resistance r_{line}, inductance L_{line}, and capacitance C_{line}. The ac-side subsystems are modeled by their Thévenin equivalent circuits where resistances $r_{s,1}$ and $r_{s,2}$, and inductances $L_{s,1}$ and $L_{s,2}$ represent the ac subsystem's Thévenin impedances. The three-phase Thévenin equivalent sources $\mathbf{e}_{abc,1}$ and $\mathbf{e}_{abc,2}$ are considered to be purely sinusoidal, whose phase a angles are indicated as $\theta_{s,1}$ and $\theta_{s,2}$ in Figure 3.1. These angles can be typically obtained by a phase-locked-loop (PLL).

For the thyristor-based LCR, the firing angle α^{LCR} can be set either manually or by a controller and is determined with respect to $\theta_{s,1}$. For the inverter side, the modulation index M^{VSC} and angle δ^{VSC} are the inputs to the gate signal generator. These values determine the amplitude

27

and angle of the fundamental component of the VSC ac voltages with regards to the dc terminal

voltage and $\theta_{s,2}$, respectively.

To define the AVM formulation, the ac variables are transformed to the qd reference frames

rotating with $\theta_{s,1}$ or $\theta_{s,2}$ using Park's transformation matrix as

$$\mathbf{v}_{qd}^{\text{LCR}} = \mathbf{K}\left(\theta_{s,1}\right)\mathbf{v}_{abc}^{\text{LCR}}, \quad \mathbf{i}_{qd}^{\text{LCR}} = \mathbf{K}\left(\theta_{s,1}\right)\mathbf{i}_{abc}^{\text{LCR}}, \tag{3.1}$$

$$\mathbf{v}_{qd}^{\text{VSC}} = \mathbf{K}\left(\theta_{s,2}\right)\mathbf{v}_{abc}^{\text{VSC}}, \quad \mathbf{i}_{qd}^{\text{VSC}} = \mathbf{K}\left(\theta_{s,2}\right)\mathbf{i}_{abc}^{\text{VSC}}, \tag{3.2}$$

where $\mathbf{K}$ is Park's transformation matrix. $\mathbf{v}_{abc}^{\text{LCR}}$, $\mathbf{i}_{abc}^{\text{LCR}}$ and $\mathbf{v}_{abc}^{\text{VSC}}$, $\mathbf{i}_{abc}^{\text{VSC}}$ are the LCR and VSC ac

voltages and currents in abc coordinates, respectively.

Also, $\mathbf{v}_{qd}^{\text{LCR}}$, $\mathbf{i}_{qd}^{\text{LCR}}$ and $\mathbf{v}_{qd}^{\text{VSC}}$, $\mathbf{i}_{qd}^{\text{VSC}}$ represent the LCR and VSC transformed qd variables.

The LCR and VSC waveforms contain significant harmonics and ripples because of the

discrete switching operation. In AVMs, the switching events are ignored, and the relation between

the average values of the dc and qd variables are established using the so-called parametric

functions for LCRs, and the modulation index M^{VSC} and angle δ^{VSC} for VSCs. Therefore, first,

fast averaging [34] should be applied to capture the average values of the qd and dc variables.

3.1.1   Indirectly-Interfaced AVMs of LCRs and VSCs

In the conventional IDI-AVMs of LCRs and VSCs, the discrete switches are substituted with

continuously controlled dependent voltage and current sources, as shown in Figure 3.2. For

parametric AVM (PAVM) of LCRs [34], the amplitude of the fundamental frequency components

of ac variables (or the average values of transformed qd variables) are related to the average values
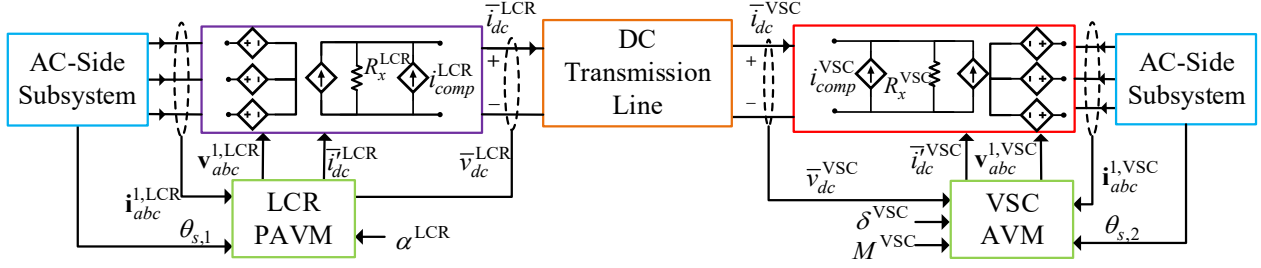
Figure 3.2 Implementation of the IDI-AVM of a hybrid LCC-VSC HVDC system using dependent voltage/current sources.

of the dc variables using so-called parametric functions $w_v^{\text{LCR}}(.)$ and $w_i^{\text{LCR}}(.)$, which are defined as [34]

$$w_v^{\text{LCR}}(.) = \frac{\left\| \bar{\mathbf{v}}_{qd}^{\text{LCR}} \right\|}{\bar{v}_{dc}^{\text{LCR}}}, \quad w_i^{\text{LCR}}(.) = \frac{\bar{i}_{dc}^{\text{LCR}}}{\left\| \bar{\mathbf{i}}_{qd}^{\text{LCR}} \right\|}. \tag{3.3}$$

Also, the relation between the angles of fundamental components of the LCR ac voltages and currents is captured by the parametric function $\varphi^{\text{LCR}}(.)$ defined as [34]

$$\varphi^{\text{LCR}}(.) = \tan^{-1}\left(\frac{\bar{i}_d^{\text{LCR}}}{\bar{i}_q^{\text{LCR}}} \right) - \tan^{-1}\left(\frac{\bar{v}_d^{\text{LCR}}}{\bar{v}_q^{\text{LCR}}} \right). \tag{3.4}$$

Two-dimensional look-up tables are utilized to store parametric functions (3.3) and (3.4) with respect to the LCR firing angle α^{LCR} and the dynamic impedance z_d^{LCR}, which specifies the LCR loading conditions and is defined as [34]

$$z_d^{\text{LCR}} = \frac{\bar{v}_{dc}^{\text{LCR}}}{\left\| \bar{\mathbf{i}}_{qd}^{\text{LCR}} \right\|}. \tag{3.5}$$

The numerical method established in [34] can be used to derive the parametric functions from simulation with the detailed switching model. To implement the PAVM of LCR, first, the

29

dynamic impedance z_d^{LCR} should be determined for the LCR operating condition using the AVM

inputs $\bar{v}_{dc}^{LCR}$ and $\bar{i}_{qd}^{LCR}$ (3.5). Then, parametric functions are obtained from look-up tables for

inputs z_d^{LCR} and α^{LCR}. Afterward, the LCR qd voltages are calculated using the parametric

functions as

$$
\begin{cases}
\bar{v}_q^{LCR} = w_v^{LCR}(.)\bar{v}_{dc}^{LCR}\cos\left(\tan^{-1}\left(\dfrac{\bar{i}_d^{LCR}}{\bar{i}_q^{LCR}}\right)-\varphi^{LCR}(.)\right) \\[4mm]
\bar{v}_d^{LCR} = w_v^{LCR}(.)\bar{v}_{dc}^{LCR}\sin\left(\tan^{-1}\left(\dfrac{\bar{i}_d^{LCR}}{\bar{i}_q^{LCR}}\right)-\varphi^{LCR}(.)\right)
\end{cases}.
\tag{3.6}
$$

By using the inverse of Park's transformation, the three-phase controlled ac voltage source of

LCR in *abc* coordinates $\mathbf{v}_{abc}^{1,LCR}$, shown in Figure 3.2, can be calculated as

$$
\mathbf{v}_{abc}^{1,LCR} = \left[\mathbf{K}(\theta_{s,1})\right]^{-1}\bar{\mathbf{v}}_{qd}^{LCR}.
\tag{3.7}
$$

Similarly, a controlled dc current source is used for interfacing with the dc-side network, and which

is calculated using the parametric function $w_i^{LCR}(.)$ as

$$
\bar{i}_{dc}^{LCR} = w_i^{LCR}(.)\left\|\bar{\mathbf{i}}_{qd}^{LCR}\right\|.
\tag{3.8}
$$

It is noted that to interface the dc current source with the dc-side subsystem, a parallel

snubber R_x^{LCR} may need to be utilized. In that case, a compensation current i_{comp}^{LCR} is used to

eliminate the steady-state error caused by the snubber. The compensation current source is

calculated as

$$
i_{comp}^{LCR} = \frac{1}{R_x^{LCR}}\left(\bar{v}_{dc}^{LCR}\big|_{t-\Delta t}\right).
\tag{3.9}
$$

The dc terminal voltage over the snubber of LCR can be calculated as

$$\bar{v}_{dc}^{LCR} = R_x^{LCR} (\bar{i}_{dc}^{LCR} + i_{comp}^{LCR} - \bar{i}_{dc}^{LCR}). \tag{3.10}$$

For AVM of VSCs, the relation between the average values of qd variables (or fundamental components of ac variables) and average values of the dc variables are defined using the modulation index M^{VSC} and angle δ^{VSC} (which may be set either manually or obtained from controllers). For sinusoidal-pulse-width-modulation (SPWM), the relation between the averaged qd output voltages $\bar{\mathbf{v}}_{qd}^{VSC}$ and the averaged dc terminal voltage $\bar{v}_{dc}^{VSC}$ is defined as

$$\frac{\left\| \bar{\mathbf{v}}_{qd}^{VSC} \right\|}{\bar{v}_{dc}^{VSC}} = \frac{1}{2} M^{VSC}. \tag{3.11}$$

Also, δ^{VSC} determines the displacement angle of VSC ac voltages with respect to $\theta_{s,2}$. Therefore, the qd voltages can be calculated using δ^{VSC} and (3.11) as

$$\begin{cases} \bar{v}_q^{VSC} = \dfrac{1}{2} M^{VSC} \bar{v}_{dc}^{VSC} \cos\left(\delta^{VSC}\right) \\ \bar{v}_d^{VSC} = \dfrac{1}{2} M^{VSC} \bar{v}_{dc}^{VSC} \sin\left(\delta^{VSC}\right) \end{cases} \tag{3.12}$$

Applying inverse of Park's matrix, the qd voltages are transformed to the abc coordinates as

$$\mathbf{v}_{abc}^{1,VSC} = \left[\mathbf{K}(\theta_{s,2})\right]^{-1} \bar{\mathbf{v}}_{qd}^{VSC}. \tag{3.13}$$

where $\mathbf{v}_{abc}^{1,VSC}$ determines the controlled three-phase ac voltage source of IDI-AVM of VSC, shown in Figure 3.2. Also, the VSC controlled dc current source can be calculated as [49]

$$\bar{i}_{dc}^{VSC} = \frac{3}{4} M^{VSC} \left\| \bar{\mathbf{i}}_{qd}^{VSC} \right\| \cos\left(\tan^{-1}\left(\frac{\bar{i}_d^{VSC}}{\bar{i}_q^{VSC}} \right) - \delta^{VSC} \right). \tag{3.14}$$

31

Similar to the LCRs, a snubber R_x^{VSC} may be needed to interface the dc current source with the dc network. In that case, i_{comp}^{VSC} is used to compensate for the steady-state error of the snubber, which is calculated as

$$i_{comp}^{\mathrm{VSC}} = \frac{1}{R_x^{\mathrm{VSC}}} (\bar{v}_{dc}^{\mathrm{VSC}}\big|_{t-\Delta t}). \qquad (3.15)$$

Also, the VSC dc terminal voltage can be computed as

$$\bar{v}_{dc}^{\mathrm{VSC}} = R_x^{\mathrm{VSC}} (\bar{i}_{dc}^{\,\prime\mathrm{VSC}} + i_{comp}^{\mathrm{VSC}} + \bar{i}_{dc}^{\,\mathrm{VSC}}). \qquad (3.16)$$

In the indirect interfacing method, the ac currents and dc terminal voltages are the inputs to the IDI-AVMs. These values are obtained from solving the ac and dc subsystems at every time step. Therefore, without an iterative solution, e.g., in PSCAD, their values from the previous time-step should be used for calculations. This one-time-step delay may result in a numerical error when simulating the system with large time steps.

3.1.2   Directly-Interfaced AVMs of LCRs and VSCs

In the direct interfacing method, the AVMs of the LCRs and VSCs are formulated in the nodal form so that their resultant matrices can be merged into the nodal matrices of the overall network

$$\mathbf{GV} = \mathbf{I}, \qquad (3.17)$$

where $\mathbf{G}$ is the conductance matrix and $\mathbf{V}$ and $\mathbf{I}$ are the voltage and current of the network, respectively. This allows the AVM equations to be solved simultaneously with the overall system without the need for an interfacing time-step delay.

To define the nodal equations of converters, first, the expression for the dc terminal voltage of LCR (i.e., $\bar{v}_{dc}^{LCR}$ in (3.10)) and VSC (i.e., $\bar{v}_{dc}^{VSC}$ (3.16)) should be substituted into (3.6) and (3.12) to express all voltages as functions of currents. Then, the dc and qd voltage equations should be linearized at $t - \Delta t$ [47]. Afterward, the voltage vector of LCR or VSC can be described as

$$\bar{\mathbf{v}} = \mathbf{R}\bar{\mathbf{i}} + \mathbf{e}_h,\qquad(3.18)$$

where $\mathbf{R}$ is the equivalent resistance matrix and $\mathbf{e}_h$ is the voltage history vector. The components of $\mathbf{R}$ can be defined as

$$R_{mn} = \left.\frac{\partial \bar{v}_m}{\partial \bar{i}_n}\right|_{t-\Delta t},\qquad(3.19)$$

where $n, m \in \{q, d, dc\}$. Therefore, using (3.19) the equivalent resistances for LCR are calculated as

$$
\begin{cases}
R_{qq}^{LCR} = \left(R_x^{LCR} w_v^{LCR}(.) \left[w_i^{LCR}(.)\cos\left(\varphi^{LCR}(.)\right) + \left(\frac{\bar{v}_{dc}^{LCR}}{R_x^{LCR}} - \bar{i}_{dc}^{LCR} \right) \times \right. \right. \\
\qquad\qquad \left. \left. \bar{i}_d^{LCR} \times \frac{\bar{i}_d^{LCR} \cos\left(\varphi^{LCR}(.)\right) - \bar{i}_q^{LCR} \sin\left(\varphi^{LCR}(.)\right)}{\left\| \bar{\mathbf{i}}_{qd}^{LCR} \right\|^3} \right] \right)\Bigg|_{t-\Delta t} \\[4ex]
R_{qd}^{LCR} = \left(R_x^{LCR} w_v^{LCR}(.) \left[w_i^{LCR}(.)\sin\left(\varphi^{LCR}(.)\right) + \left(\frac{\bar{v}_{dc}^{LCR}}{R_x^{LCR}} - \bar{i}_{dc}^{LCR} \right) \times \right. \right. \\
\qquad\qquad \left. \left. \bar{i}_q^{LCR} \times \frac{\bar{i}_q^{LCR} \sin\left(\varphi^{LCR}(.)\right) - \bar{i}_d^{LCR} \cos\left(\varphi^{LCR}(.)\right)}{\left\| \bar{\mathbf{i}}_{qd}^{LCR} \right\|^3} \right] \right)\Bigg|_{t-\Delta t} \\[4ex]
R_{qdc}^{LCR} = \left(-R_x^{LCR} w_v^{LCR}(.)\cos\left(\tan^{-1}\left(\frac{\bar{i}_d^{LCR}}{\bar{i}_q^{LCR}} \right) - \varphi^{LCR}(.) \right) \right)\Bigg|_{t-\Delta t}
\end{cases},\qquad(3.20)
$$

$$
\begin{cases}
R_{dq}^{LCR} = -\left(R_x^{LCR} w_v^{LCR}(.) \left[w_i^{LCR}(.) \sin\left(\varphi^{LCR}(.)\right) + \left(\dfrac{\overline{v}_{dc}^{LCR}}{R_x^{LCR}} - \overline{i}_{dc}^{LCR} \right) \times \right. \right. \\
\qquad\qquad \left. \left. \overline{i}_d^{LCR} \times \dfrac{\overline{i}_d^{LCR} \times \sin\left(\varphi^{LCR}(.)\right) + \overline{i}_q^{LCR} \cos\left(\varphi^{LCR}(.)\right)}{\left\| \overline{\mathbf{i}}_{qd}^{LCR} \right\|^3} \right] \right)\Bigg|_{t-\Delta t} \\[2em]
R_{dd}^{LCR} = \left(R_x^{LCR} w_v^{LCR}(.) \left[w_i^{LCR}(.) \cos\left(\varphi^{LCR}(.)\right) + \left(\dfrac{\overline{v}_{dc}^{LCR}}{R_x^{LCR}} - \overline{i}_{dc}^{LCR} \right) \times \right. \right. \\
\qquad\qquad \left. \left. \overline{i}_q^{LCR} \times \dfrac{\overline{i}_q^{LCR} \times \cos\left(\varphi^{LCR}(.)\right) + \overline{i}_d^{LCR} \times \sin\left(\varphi^{LCR}(.)\right)}{\left\| \overline{\mathbf{i}}_{qd}^{LCR} \right\|^3} \right] \right)\Bigg|_{t-\Delta t} \\[2em]
R_{ddc}^{LCR} = \left(-R_x^{LCR} w_v^{LCR}(.) \sin\left(\tan^{-1}\left(\dfrac{\overline{i}_d^{LCR}}{\overline{i}_q^{LCR}} \right) - \varphi^{LCR}(.) \right) \right)\Bigg|_{t-\Delta t}
\end{cases} , \qquad (3.21)
$$

$$
\begin{cases}
R_{dcq}^{LCR} = \left(\dfrac{R_x^{LCR} w_v^{LCR}(.) \overline{i}_q^{LCR}}{\left\| \overline{\mathbf{i}}_{qd}^{LCR} \right\|} \right)\Bigg|_{t-\Delta t} , \quad
R_{dcd}^{LCR} = \left(\dfrac{R_x^{LCR} w_v^{LCR}(.) \overline{i}_d^{LCR}}{\left\| \overline{\mathbf{i}}_{qd}^{LCR} \right\|} \right)\Bigg|_{t-\Delta t} \\[1.5em]
R_{dcdc}^{LCR} = -R_x^{LCR}
\end{cases} . \qquad (3.22)
$$

Using Park's transformation for LCR qd impedances[47], the equivalent resistances in abc coordinates can be obtained as

$$
\mathbf{R}_{abc}^{LCR} = \left[\mathbf{K}(\theta_{s,1}) \right]^{-1} \begin{bmatrix} R_{qq}^{LCR} & R_{qd}^{LCR} \\ R_{dq}^{LCR} & R_{dd}^{LCR} \end{bmatrix} \left[\mathbf{K}(\theta_{s,1}) \right] . \qquad (3.23)
$$

Also, the *abc* to dc impedances are defined as

$$
\mathbf{R}_{abc,dc}^{LCR} = \left[\mathbf{K}(\theta_{s,1}) \right]^{-1} \begin{bmatrix} R_{qdc}^{LCR} \\ R_{ddc}^{LCR} \end{bmatrix} . \qquad (3.24)
$$

Likewise, the dc to *abc* impedances of LCR can be obtained from

$$
\mathbf{R}_{dc,abc}^{LCR} = -\left(\begin{bmatrix} R_{dcq}^{LCR} & R_{dcd}^{LCR} \end{bmatrix} \left[\mathbf{K}(\theta_{s,1}) \right] \right) . \qquad (3.25)
$$

The minus sign in (3.25) is due to the direction of the LCR dc current, which is considered outward of the component. Finally, the impedance matrix for the *abc*-dc nodes of LCR is defined as

$$\mathbf{R}_{\text{LCR}} = \begin{bmatrix} \mathbf{R}_{abc}^{\text{LCR}} & \mathbf{R}_{abc,dc}^{\text{LCR}} \\ \mathbf{R}_{dc,abc}^{\text{LCR}} & R_{dcdc}^{\text{LCR}} \end{bmatrix}. \tag{3.26}$$

Also, the *qd*-dc voltage history terms of LCR can be calculated as

$$\begin{cases} e_{hq}^{\text{LCR}} = \left(w_v^{\text{LCR}}(.)\overline{v}_{dc}^{\text{LCR}} \cos\left(\tan^{-1}\left(\dfrac{\overline{i}_d^{\text{LCR}}}{\overline{i}_q^{\text{LCR}}} \right) - \varphi^{\text{LCR}}(.) \right) \right)\Big|_{t-\Delta t} \\[4ex] e_{hd}^{\text{LCR}} = \left(w_v^{\text{LCR}}(.)\overline{v}_{dc}^{\text{LCR}} \sin\left(\tan^{-1}\left(\dfrac{\overline{i}_d^{\text{LCR}}}{\overline{i}_q^{\text{LCR}}} \right) - \varphi^{\text{LCR}}(.) \right) \right)\Big|_{t-\Delta t} \\[4ex] e_{hdc}^{\text{LCR}} = \overline{v}_{dc}^{\text{LCR}}\Big|_{t-\Delta t} \end{cases} \tag{3.27}$$

The *qd* voltage history terms should be transferred to *abc* coordinates using

$$\mathbf{e}_{habc}^{\text{LCR}} = \left[\mathbf{K}(\theta_{s,1}) \right]^{-1} [e_{hq}^{\text{LCR}} \quad e_{hd}^{\text{LCR}}]^T. \tag{3.28}$$

The vector of *abc*-dc LCR voltage history terms $\mathbf{e}_{hLCR}$ is defined as

$$\mathbf{e}_{hLCR} = [\mathbf{e}_{habc}^{\text{LCR}} \quad e_{dc}^{\text{LCR}}]^T. \tag{3.29}$$

Finally, the Norton equivalent of the DI-AVM of LCR can be defined

$$\mathbf{G}_{\text{LCR}} = \left[\mathbf{R}_{\text{LCR}} \right]^{-1}, \quad \mathbf{I}_{hLCR} = -\left[\mathbf{R}_{\text{LCR}} \right]^{-1} \mathbf{e}_{hLCR}, \tag{3.30}$$

where $\mathbf{G}_{\text{LCR}}$ is the conductance matrix and $\mathbf{I}_{hLCR}$ is the current history vector of LCR.

Using the same approach, the equivalent resistances for VSC are computed by linearizing the *qd* and dc voltage equations which results in [49]

$$
\begin{cases}
R_{qq}^{\text{VSC}} = \dfrac{3}{8}(M^{\text{VSC}})^2 R_x^{\text{VSC}} \cos^2(\delta^{\text{VSC}}), R_{qd}^{\text{VSC}} = \dfrac{3}{16}(M^{\text{VSC}})^2 R_x^{\text{VSC}} \sin(2\delta^{\text{VSC}}) \\[2mm]
R_{qdc}^{\text{VSC}} = \dfrac{1}{2}M^{\text{VSC}} R_x^{\text{VSC}} \cos(\delta^{\text{VSC}}), R_{dq}^{\text{VSC}} = \dfrac{3}{16}(M^{\text{VSC}})^2 R_x^{\text{VSC}} \sin(2\delta^{\text{VSC}}) \\[2mm]
R_{dd}^{\text{VSC}} = \dfrac{3}{8}(M^{\text{VSC}})^2 R_x^{\text{VSC}} \sin^2(\delta^{\text{VSC}}), R_{ddc}^{\text{VSC}} = \dfrac{1}{2}M^{\text{VSC}} R_x^{\text{VSC}} \sin(\delta^{\text{VSC}}) \\[2mm]
R_{dcq}^{\text{VSC}} = \dfrac{3}{4}M^{\text{VSC}} R_x^{\text{VSC}} \cos(\delta^{\text{VSC}}), R_{dcd}^{\text{VSC}} = \dfrac{3}{4}M^{\text{VSC}} R_x^{\text{VSC}} \sin(\delta^{\text{VSC}}) \\[2mm]
R_{dcdc}^{\text{VSC}} = R_x^{\text{VSC}}
\end{cases}
\tag{3.31}
$$

Similar to the LCR, the *abc*-dc resistances of VSC can be calculated as

$$
\mathbf{R}_{abc}^{\text{VSC}} = \left[\mathbf{K}(\theta_{s,2}) \right]^{-1}
\begin{bmatrix}
R_{qq}^{\text{VSC}} & R_{qd}^{\text{VSC}} \\
R_{dq}^{\text{VSC}} & R_{dd}^{\text{VSC}}
\end{bmatrix}
\left[\mathbf{K}(\theta_{s,2}) \right],
\tag{3.32}
$$

$$
\mathbf{R}_{abc,dc}^{\text{VSC}} = \left[\mathbf{K}(\theta_{s,2}) \right]^{-1}
\begin{bmatrix}
R_{qdc}^{\text{VSC}} \\
R_{ddc}^{\text{VSC}}
\end{bmatrix},
\tag{3.33}
$$

$$
\mathbf{R}_{dc,abc}^{\text{VSC}} = (\mathbf{R}_{abc,dc}^{\text{VSC}})^T .
\tag{3.34}
$$

Using the obtained sub-matrices, the impedance matrix of VSC is defined as

$$
\mathbf{R}_{\text{VSC}} =
\begin{bmatrix}
\mathbf{R}_{abc}^{\text{VSC}} & \mathbf{R}_{abc,dc}^{\text{VSC}} \\
\mathbf{R}_{dc,abc}^{\text{VSC}} & R_{dcdc}^{\text{VSC}}
\end{bmatrix}.
\tag{3.35}
$$

Also, the voltage history terms for *qd*-dc and *abc*-dc can be similarly calculated as [49]

$$
\begin{cases}
e_{hq}^{\text{VSC}} = \dfrac{1}{2}M^{\text{VSC}} \cos(\delta^{\text{VSC}}) \bar{v}_{dc}^{\text{VSC}} \Big|_{t-\Delta t} \\[2mm]
e_{hd}^{\text{VSC}} = \dfrac{1}{2}M^{\text{VSC}} \sin(\delta^{\text{VSC}}) \bar{v}_{dc}^{\text{VSC}} \Big|_{t-\Delta t} \\[2mm]
e_{hdc}^{\text{VSC}} = \bar{v}_{dc}^{\text{VSC}} \Big|_{t-\Delta t}
\end{cases}
,
\tag{3.36}
$$

$$
\mathbf{e}_{habc}^{\text{VSC}} = \left[\mathbf{K}(\theta_{s,2}) \right]^{-1} [e_{hq}^{\text{VSC}} \quad e_{hd}^{\text{VSC}}]^T ,
\tag{3.37}
$$

$$\mathbf{e}_{h\text{VSC}} = \begin{bmatrix} \mathbf{e}_{habc}^{\text{VSC}} & e_{hdc}^{\text{VSC}} \end{bmatrix}^T. \tag{3.38}$$

Finally, the Norton interface of DI-AVM of VSC is defined as

$$\mathbf{G}_{\text{VSC}} = \begin{bmatrix} \mathbf{R}_{\text{VSC}} \end{bmatrix}^{-1}, \quad \mathbf{I}_{h\text{VSC}} = -\begin{bmatrix} \mathbf{R}_{\text{VSC}} \end{bmatrix}^{-1} \mathbf{e}_{h\text{VSC}}, \tag{3.39}$$

where $\mathbf{G}_{\text{VSC}}$ is the conductance matrix and $\mathbf{I}_{h\text{VSC}}$ is the current history vector of VSC.

Once the equivalent conductance matrix and history current sources are obtained for LCR and VSC, their DI-AVM can be implemented either using coupled resistors and dependent voltage/current sources (see [47], Fig. 5), or directly coded in the program as user-defined blocks.

3.2   Performance Verification

To validate the numerical performance of the presented DI-AVMs of LCC and VSC, the hybrid LCC-VSC HVDC system in Figure 3.1 is considered for study, with parameters summarized in Appendix C . The system has been implemented in PSCAD/EMTDC using three different models of the LCR and VSC including: the detailed switching model, IDI-AVM, and DI-AVM. Also, the solution of the IDI-AVM achieved with the small time-step of 1μs is considered as the reference.

It is assumed that the system is initially operating in a steady-state with the LCR firing angle α^{LCR} set to 15 degrees. Also, the modulation index M^{VSC} and angle δ^{VSC} are set to 0.8 and -57.29 degrees, respectively. The transferred active and reactive power to the receiving end is 1350 MW and -225 MVAR, respectively. At t=3s, the modulation index M^{VSC} is stepped down to 0.6, which increases the active power to 1460 MW. Also, the reactive power changes to -196 MVAR. Then, at t=8s, angle δ^{VSC} is changed to -67.03 degrees to achieve the active power of
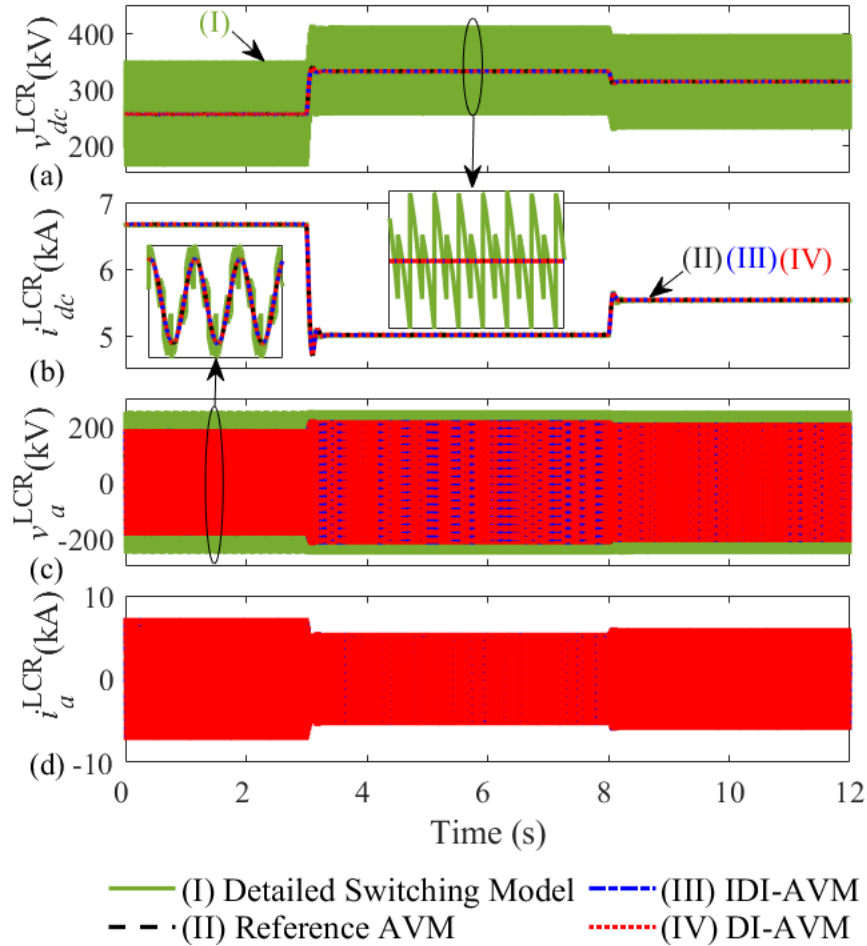
Figure 3.3 Transient response of ac and dc variables of the LCR in the sending end of the hybrid HVDC system as obtained by the subject models for: (a) LCR dc voltage, (b) LCR dc current, (c) LCR phase a voltage, and (d) LCR phase a current. Here, IDI-AVM and DI-AVM are run with 10 μs.

1500 MW and zero reactive power. The transient response of the system is presented in Figure 3.3 and Figure 3.4 for some of the LCR and VSC variables, respectively, where both IDI-AVM and DI-AVM are executed with the time step of 10 μs.

It can be noted from Figure 3.3 and Figure 3.4 that, with such small time-step sizes, both DI-AVM and IDI-AVM are able to accurately reconstruct the average values of the dc-side variables and fundamental components of ac-side variables consistently with the reference AVM.

38
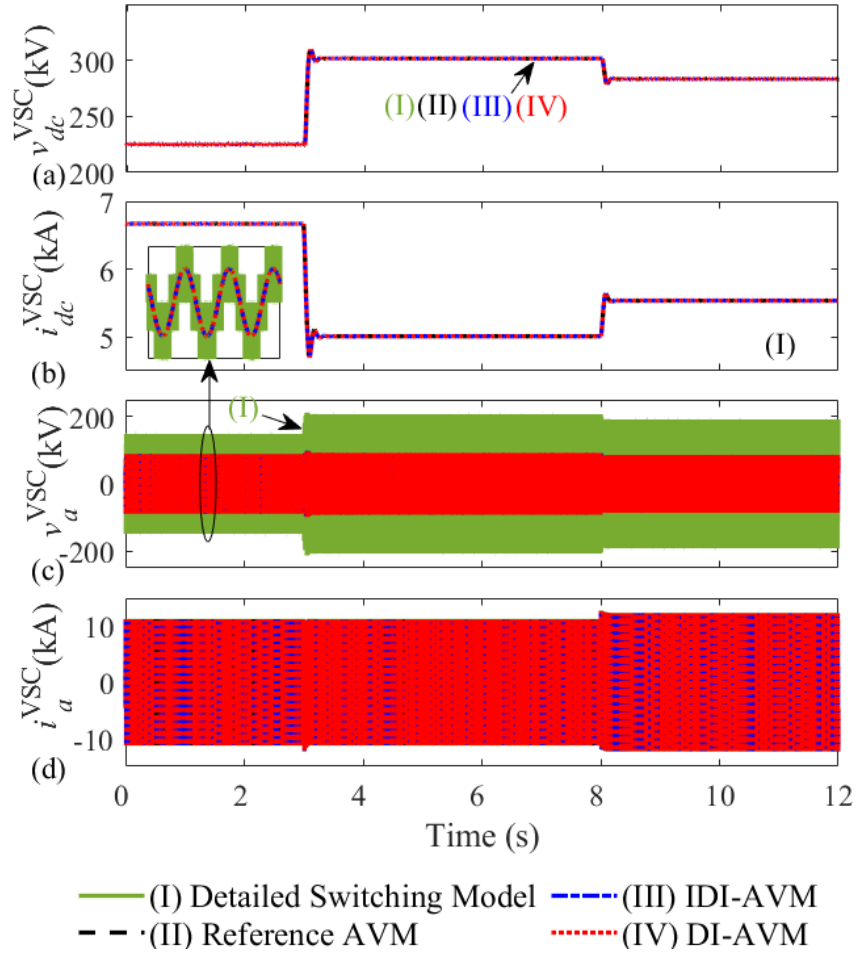
Figure 3.4 Transient response of ac and dc variables of the VSC in the receiving end of the hybrid HVDC system as obtained by the subject models for: (a) VSC dc voltage, (b) VSC dc current, (c) VSC phase a voltage, and (d) VSC phase a current. Here, IDI-AVM and DI-AVM are run with 10 μs.

The results of AVMs are also in agreement with the results of the detailed switching model if the switching ripples are neglected.

To show the superiority of the DI-AVM over the IDI-AVM, the same study is conducted with larger simulation time steps. For this purpose, IDI-AVM is simulated with a time-step of 150 μs and the DI-AVM is run with 500 μs which is a much larger time-step size. The magnified view of the transient response of several variables is shown in Figure 3.5, as obtained by the subject

39
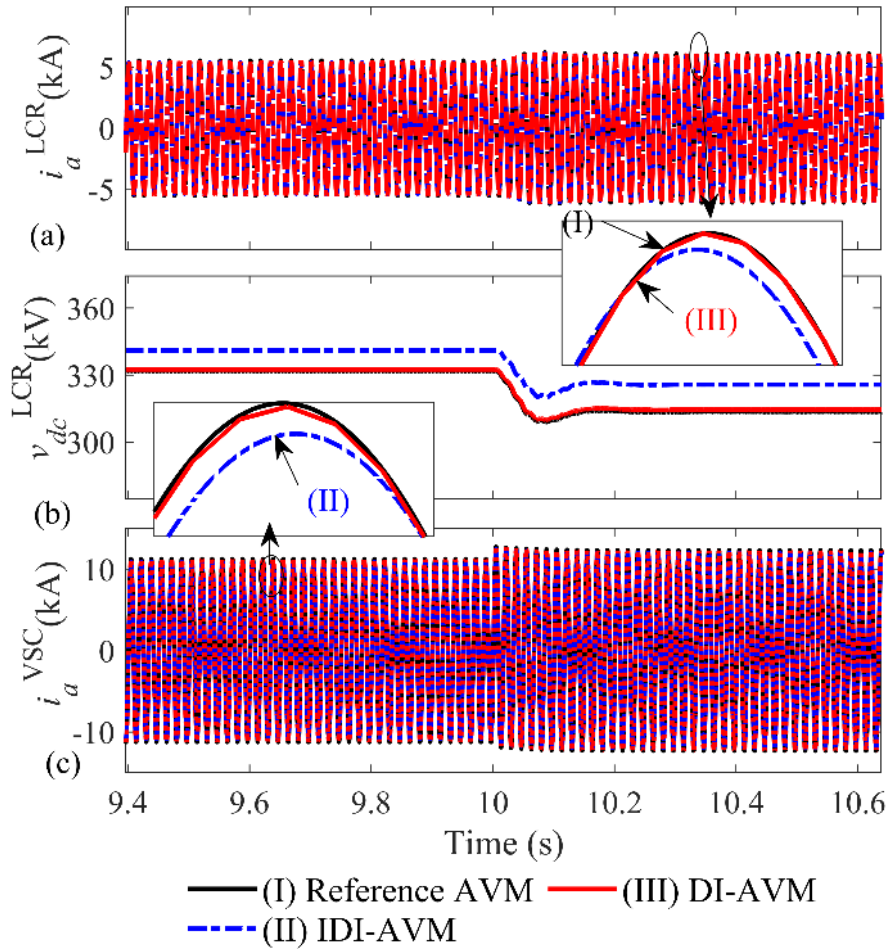
Figure 3.5 Magnified view of the transient response of several variables of the hybrid HVDC system as obtained by the subject models for: (a) LCR phase a current, (b) LCR dc voltage, (c) VSC phase a current. Here, IDI-AVM is run with 150 μs and DI-AVM is run with 500 μs.

models. It can be noted in Figure 3.5 that the solution of the IDI-AVM visibly diverges from the reference at 150 μs due to the error caused by the one time-step interfacing delay. Meanwhile, the DI-AVM can provide very accurate results compared to the reference solution even with time-step sizes as large as 500 μs.

Chapter 4: Detailed Parametric Modeling of AC–DC Converters for EMT Simulators

As mentioned for the HPAVM, the challenge of solving duplicate networks for average values and ripples/harmonics leads to increased computational costs. As an alternative, fast dynamic averaging can be employed, as depicted in Figure 4.1(a). This approach involves solving a single network, and the inputs for the HPAVM are acquired through averaging. While this method reduces computational burden by necessitating only a single network, the accuracy of solutions during transient periods is compromised, as shown in Figure 4.2, due to the inherent effects of averaging.

Furthermore, in the HPAVM and all preceding methodologies that account for ripples/harmonics, the reliance on average values prevents the models from distinguishing between distinct compositions within the dc network in terms of ripples/harmonics. Consequently, the precision of ripples/harmonics is confined to the specific system on which the lookup tables are constructed. (i.e., if lookup tables are derived from a purely resistive dc network, the model's capability is limited to reproducing ripples solely for resistive dc loads.)

This Chapter proposes a new parametric detailed non-switching model (DNSM) for the widely-used 2-level ac-dc converters, i.e., LCRs and VSCs. The proposed DNSM is able to reconstruct the ac and dc waveforms similar to the DSMs of converters, including all harmonics and ripples. This is achieved by formulating the parametric functions that are defined based on the instantaneous values of ac and dc variables. As opposed to the HPAVM, the ac harmonics and the dc ripples are computed with their fundamental frequency components and average values,
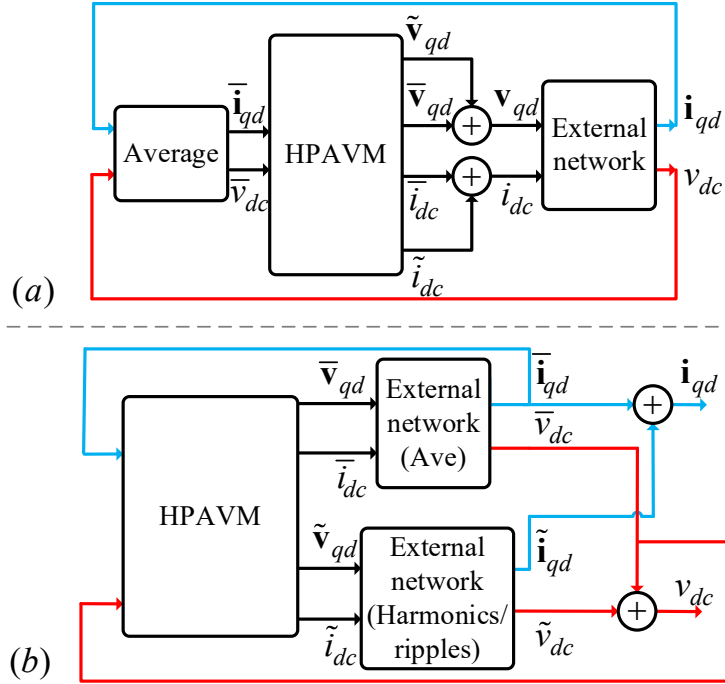
Figure 4.1 Implementation of the HPAVM: (a) using fast dynamic averaging, and (b) duplicating the network.

(I) Detailed Switching — — — (III) HPAVM (method I)
— — — (II) HPAVM (method II)
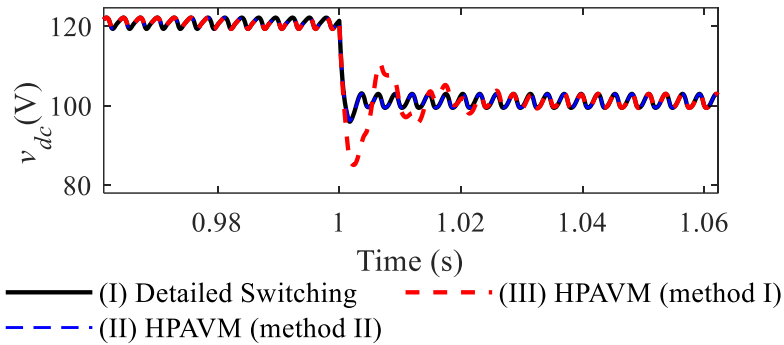
Figure 4.2 dc terminal voltage waveforms obtained by: (I) the conventional detailed switching models, (II) HPAVM with duplicating the network (III) HPAVM with fast dynamic averaging.

respectively. Here, two interfacing methodologies for DNSM, denoted as indirectly-interfaced DNSM (IDI-DNSM), which uses a time-step relaxation, and directly-interfaced DNSM (DI-
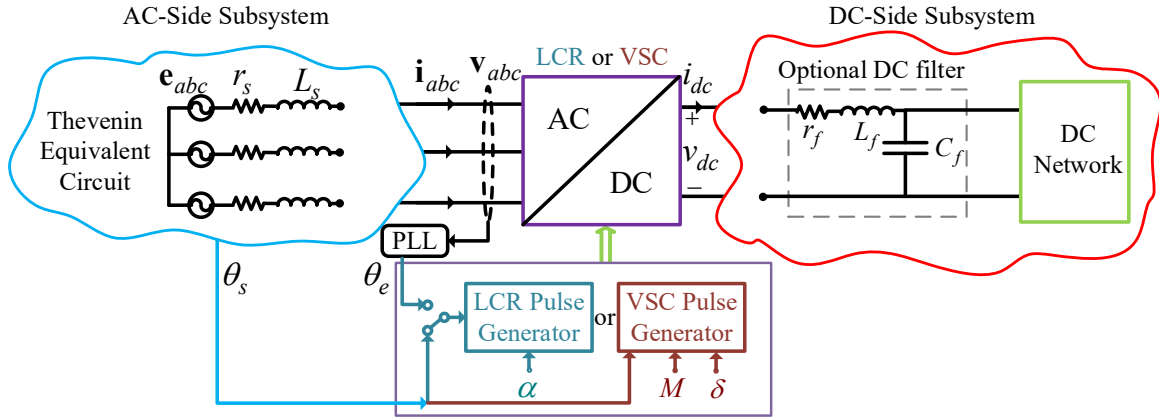
Figure 4.3 A generic ac–dc converter system consisting of an LCR or VSC.

DNSM), which uses linearization and simultaneous solution, are formulated. The advantages of the proposed models over the DSMs are demonstrated on generic LCRs and VSCs implemented in PSCAD (offline simulations) and RSCAD (real-time simulations using NovaCor of RTDS). It is verified that IDI-DNSM and DI-DNSM allow much larger simulation time steps compared to the conventional DSMs while providing accurate waveforms for ac and dc variables.

4.1   Detailed Parametric Model of AC-DC Converters

Without loss of generality, a generic three-phase 2-level ac–dc conversion system depicted in Figure 4.3 is considered to define the proposed methodology. The ac and dc subsystems are interconnected by either a six-pulse LCR (composed of diode or thyristor switches) or a VSC (composed of forced-commutated transistors, e.g., IGBTs). The dc subsystem may consist of a dc network and an optional low-pass filter to smoothen the dc terminal voltage. The ac subsystem may include rotating electrical machines, ac filters, ac loads, transmission lines, etc. The Thévenin
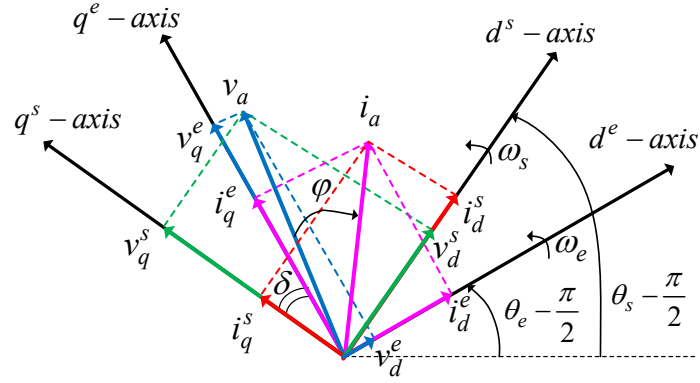
Figure 4.4 Vector diagram of the converter ac currents and voltages in two qd reference frames rotating with angles of ac sources and converter terminal voltages.

equivalent is utilized to represent the ac subsystem where equivalent voltages $\mathbf{e}_{abc}$ are assumed to be balanced and sinusoidal as

$$\mathbf{e}_{abc} = \sqrt{2}\, E_{\text{rms}} \left[\cos(\theta_s) \quad \cos(\theta_s - \frac{2\pi}{3}) \quad \cos(\theta_s + \frac{2\pi}{3}) \right]^T . \tag{4.1}$$

Here, E_{rms} is the rms value of phase voltages, and θ_s indicates the angle of phase a of the equivalent ac sources. The ac side Thévenin equivalent impedance is represented by r_s and L_s. The converter terminal voltages are denoted by $\mathbf{v}_{abc}$ whose fundamental frequency component has the angle

$$\theta_e = \int \left(2\pi f_e \right) dt , \tag{4.2}$$

where f_e is the frequency of the ac subsystem in Hz. The angles θ_e and θ_s are related as

$$\delta = \theta_s - \theta_e , \tag{4.3}$$

where δ is referred to as the power transfer angle.

As depicted in Figure 4.3, the firing angle α and angle θ_s, or θ_e, are the inputs into the firing pulse generator for the thyristor-based LCRs. The firing angle α may be computed based

on either the angle θ_s or θ_e, which can be identified by a phase-locked-loop (PLL). For the VSC, the modulation index M, angle δ, and angle θ_s are the inputs into the pulse generator. Here, δ is used to specify the angle of the fundamental frequency component of the VSC ac voltages θ_e based on (4.3). Also, the modulation index M determines the amplitude of the fundamental frequency component of VSC ac voltages with respect to the dc terminal voltage.

4.1.1   Formulation of DSNM

For the purpose of derivation, the converter ac voltages $\mathbf{v}_{abc}$ and currents $\mathbf{i}_{abc}$ are transformed to the source qd synchronous reference frame with angle θ_s, as shown in Figure 4.4, and computed using Park's transformation matrix $\mathbf{K}$ [56] as

$$\mathbf{v}_{qd}^s = \mathbf{K}(\theta_s)\mathbf{v}_{abc}, \qquad \mathbf{i}_{qd}^s = \mathbf{K}(\theta_s)\mathbf{i}_{abc}, \tag{4.4}$$

where $\mathbf{v}_{qd}^s$ and $\mathbf{i}_{qd}^s$ are the transformed ac variables. In the source qd reference frame, the axis q^s is aligned with the phase a of the equivalent source voltages $\mathbf{e}_{abc}$.

Typical waveforms of dc and transformed qd ac variables for the LCR-based ac-dc system in Figure 4.3 are illustrated in Figure 4.5. As seen in Figure 4.5, similar to the dc-side variables, the transformed qd ac variables are also composed of dc average values and oscillatory components (i.e., ripples) which correspond to the sum of all the ac harmonics in the abc coordinates. Also, the dc average values of qd variables correspond to the amplitude of the fundamental frequency component of the ac variables in the abc coordinates.
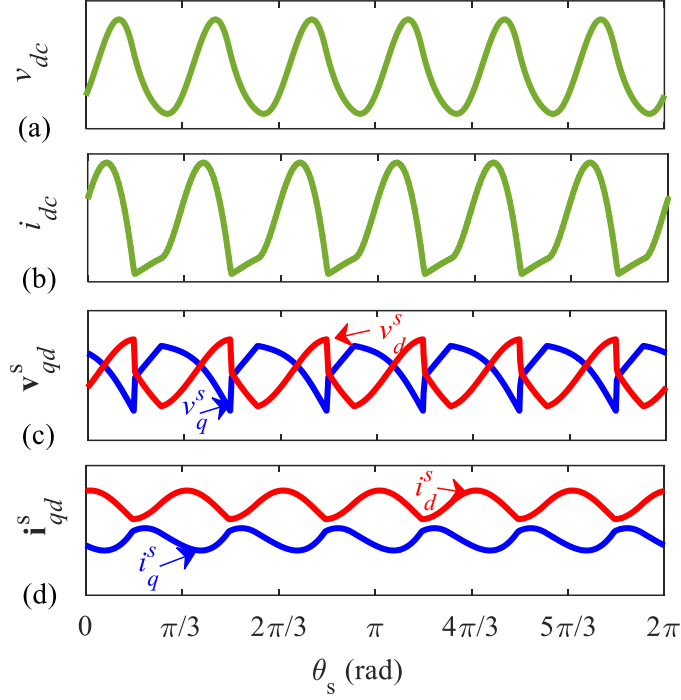
Figure 4.5 Typical waveforms of terminal variables for six-pulse LCRs over one ac cycle: (a) dc voltage, (b) dc current, (c) ac transformed *qd* voltages, (d) ac transformed *qd* currents.

In the VSC-based system, the dc and *qd* variables also contain dc average values and ripples generated by the high-frequency switching. Their average values will correspond to the fundamental frequency components, and the ripples will correspond to the ac harmonics.

The proposed technique uses parametric functions to capture the relationships between the entire waveforms of the dc and *qd* ac variables. As opposed to the PAVM [34], GPAVM [44], and HPAVM [45], in the proposed DNSM, these relationships are formulated based upon the instantaneous values of the dc and *qd* ac variables/waveforms, containing both the average values and oscillatory ripples. For this purpose, a parametric function $w_i(.)$ is defined as

$$w_i(.) = \frac{i_{dc}}{\left\| \mathbf{i}_{qd}^s \right\|},$$

(4.5)

46

which at any moment relates the instantaneous values of the dc current and the magnitude of the

qd ac currents. Similarly, a parametric function $w_v(.)$ is defined as

$$w_v(.) = \frac{\left\| \mathbf{v}_{qd}^s \right\|}{v_{dc}}, \tag{4.6}$$

which at any moment relates the instantaneous values of the dc voltage and the magnitude of the

qd ac voltages.

The phase shift between the instantaneous angles of the ac currents and ac voltages is also

captured with a parametric function $\varphi(.)$ defined as

$$\varphi(.) = \tan^{-1}\left(\frac{i_d^s}{i_q^s} \right) - \tan^{-1}\left(\frac{v_d^s}{v_q^s} \right). \tag{4.7}$$

The parametric functions (4.5)–(4.7) are defined at any moment and for the desired operating

conditions of the ac-dc converter. For this purpose, the loading condition of the converter is

specified by defining an instantaneous dynamic impedance as

$$z_d = \frac{v_{dc}}{\left\| \mathbf{i}_{qd}^s \right\|}. \tag{4.8}$$

The profiles of the parametric functions $w_i(.)$, $w_v(.)$, $\varphi(.)$, and z_d calculated based on the

typical waveforms in Figure 4.5 for the LCR system are depicted in Figure 4.6 over one ac cycle.

It is observed that these functions are also periodic similar to the ripples on the dc and qd ac

variables when considering their instantaneous values. The period of these ripples for LCR-based

system is obtained as
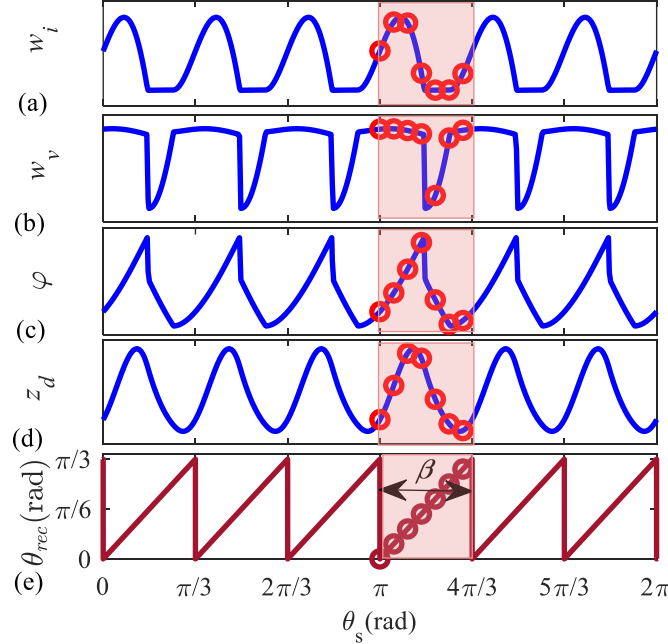
Figure 4.6 Typical waveforms of the instantaneous parametric functions and dynamic impedance of the LCR-based system for the proposed DNSM over one ac cycle: (a) parametric function $w_i(.)$ defined in (4.5), (b) parametric function $w_v(.)$ defined in (4.6), (c) parametric function $\varphi(.)$ defined in (4.7), (d) dynamic impedance z_d defined in (4.8), (e) reconstruction angle defined in (4.11).

$$\beta = 2\pi / p, \tag{4.9}$$

where p denotes the number of LCR pulses (in Figure 4.5 and 4 $p=6$).

For VSCs, the period of ripples β on the dc and qd variables, and parametric functions is equal. However, β of VSCs will also depend on the switching strategy, unsynchronized or synchronized carrier frequency, symmetry or asymmetry of the carrier about a sinusoidal reference waveform of SPWM, etc.[1], [57].

In this Chapter, a synchronous modulation with odd and multiple of 3 switching frequency ratio is considered to eliminate the even and triple harmonics, and the harmonics of the order of
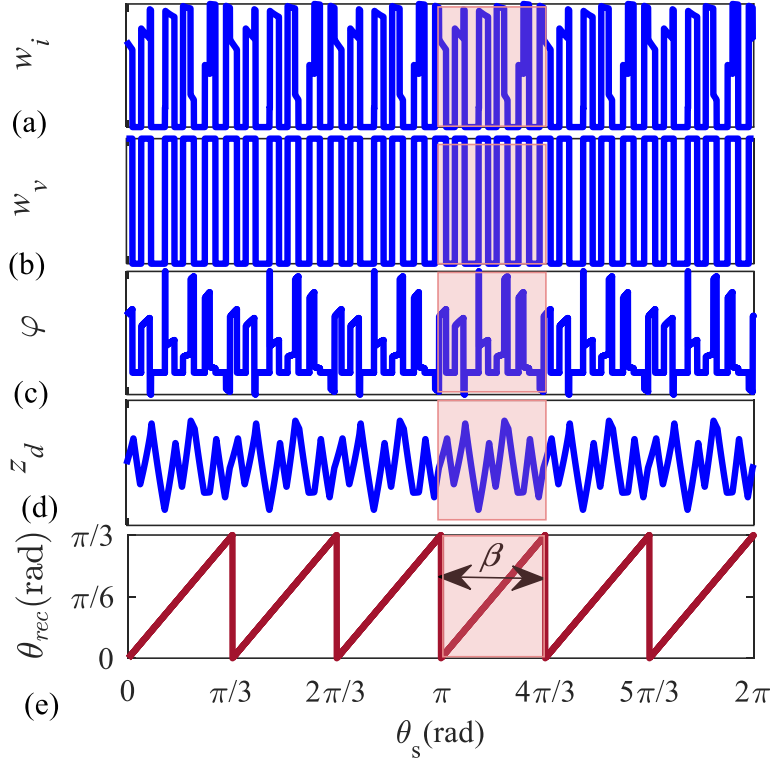
Figure 4.7 Typical waveforms of the instantaneous parametric functions and dynamic impedance of the VSC-based system in specific modulation index and angle for the proposed DNSM over one ac cycle: (a) parametric function $w_i(.)$ defined in (4.5), (b) parametric function $w_v(.)$ defined in (4.6), (c) parametric function $\varphi(.)$ defined in (4.7), (d) dynamic impedance z_d defined in (4.8), (e) reconstruction angle defined in (4.11).

the carrier frequency, resulting in the ac harmonic order of [58]

$$n = 6m \pm 1, \quad m \in \{1, 2, 3, \ldots\}, \tag{4.10}$$

which results in harmonic order of $6m$ on dc and qd variables. Therefore, the period of ripples is specified as $\beta = \dfrac{\pi}{3}$ for the subject VSC system [58] .

After determining the period β, adequate samples of the parametric functions can be

collected over only one period β as illustrated in Figure 4.6. For this purpose, the so-called reconstruction angle θ_{rec} is defined as

$$\theta_{rec} = \mathrm{mod}\left(\theta_s / \beta\right). \tag{4.11}$$

The profile of θ_{rec} is shown in Figure 4.6(e).

4.1.2   Establishing Parametric Functions

It is generally impractical to derive the instantaneous parametric functions (4.5)–(4.7) analytically under various operating conditions, especially when considering the nonlinearity and losses of the converter. Here, Algorithm 1 is used for establishing the parametric functions of the LCR-based ac-dc system numerically. A similar approach is used for constructing parametric functions of the VSC-based system.

In this approach, the system is simulated using the DSM of the converter for short periods of time over different loading conditions, and the parametric functions are computed numerically. As shown in Algorithm 1, the system is simulated over the desired range of firing angles (in the case of thyristor-based LCR) denoted by its minimum α_{min} and maximum α_{max} values with step α_{step}.

The system is also simulated over the desired range of loading conditions. Here, the loading condition is varied by changing the load in the dc network, which is represented by an equivalent resistance R_l, which steps with $R_{l,step}$ from minimum $R_{l,min}$ to maximum $R_{l,max}$. It is important to note that the parametric functions obtained by varying a resistive load in the dc network are also valid for other load compositions in the dc networks, such as inductive loads.

Algorithm 1. Algorithm for construction of lookup tables

1. **for** $\alpha = \alpha_{\min}$ **to** $\alpha_{\max}$ **step** α_{step} **do**
2. **for** $R_l = R_{l,\min}$ **to** $R_{l,\max}$ **step** $R_{l,\text{step}}$ **do**
3. Initialize the system with α and R_l using DSM for LCR
4. Start the simulation
5. **for** $k = 0$ **to** N **step** 1 **do**
6. Establish θ_{rec} based on (4.11)
7. Compute functions $w_i(.)$, $w_v(.)$, $\varphi(.)$ based on (4.5)-(4.7)
8. Compute dynamic impedance z_d based on (4.8)
9. Store the parametric functions in 3-D lookup tables in terms of z_d, α, θ_{rec}
10. **end for**
11. End the simulation
12. **end for**
13. **end for**

Once the simulations start, the parametric functions are computed based on (4.5)–(4.7). Also, the dynamic impedance z_d and the reconstruction angle θ_{rec} are also established based on (4.8), (4.11), respectively, for that operating condition. Then, N samples of the parametric functions are collected over one period β, and stored in three-dimensional (3-D) lookup tables in terms of α (for thyristor-based LCR) , z_d, and θ_{rec}. Typical profiles of instantaneous dynamic impedance and parametric functions for the proposed DNSM of a diode rectifier are shown in Figure 4.8, and Figure 4.9, respectively.

For the VSC system, applying the same Algorithm 1, four-dimensional (4-D) lookup tables in terms of modulation index M, angle δ, z_d, and θ_{rec} are constructed and stored as the instantaneous parametric functions over the desired range of operation. Figure 4.10 and Figure 4.11 depict the dynamic impedance and parametric functions of a VSC system for a specific modulation index M, angle δ.
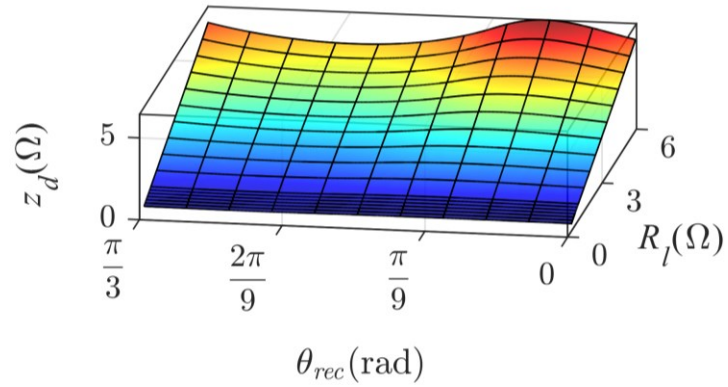
Figure 4.8 Typical dynamic impedance for the proposed DNSM of a diode rectifier.
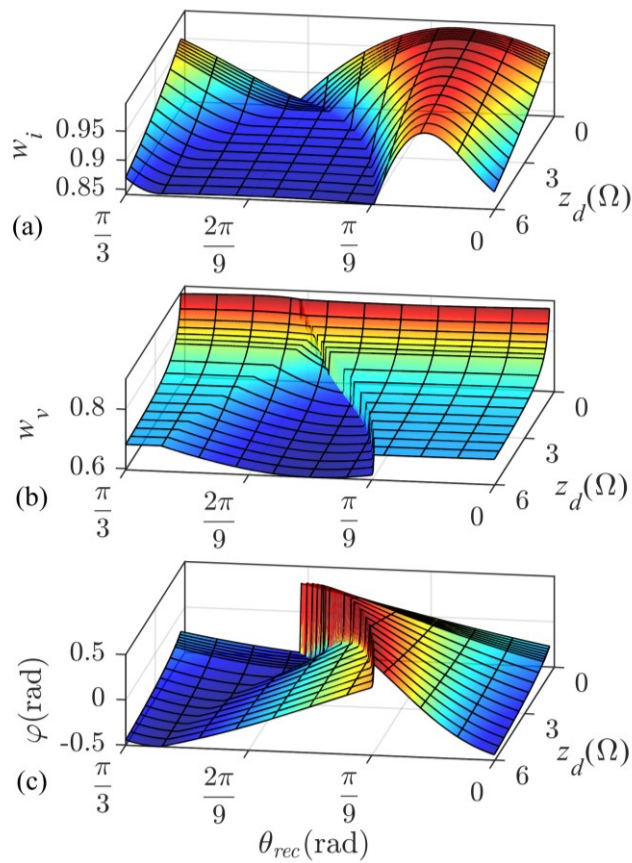
Figure 4.9 Typical parametric functions for the proposed DNSM of a diode rectifier stored in lookup tables:

(a) $w_i(.)$, **(b)** $w_v(.)$, **and (c)** $\varphi(.)$.
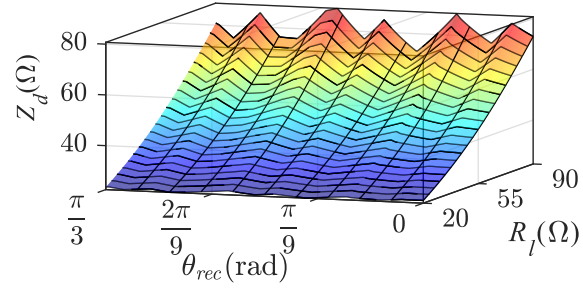
Figure 4.10 Typical dynamic impedance for the proposed DNSM of a VSC with for a specific modulation index M, angle δ.
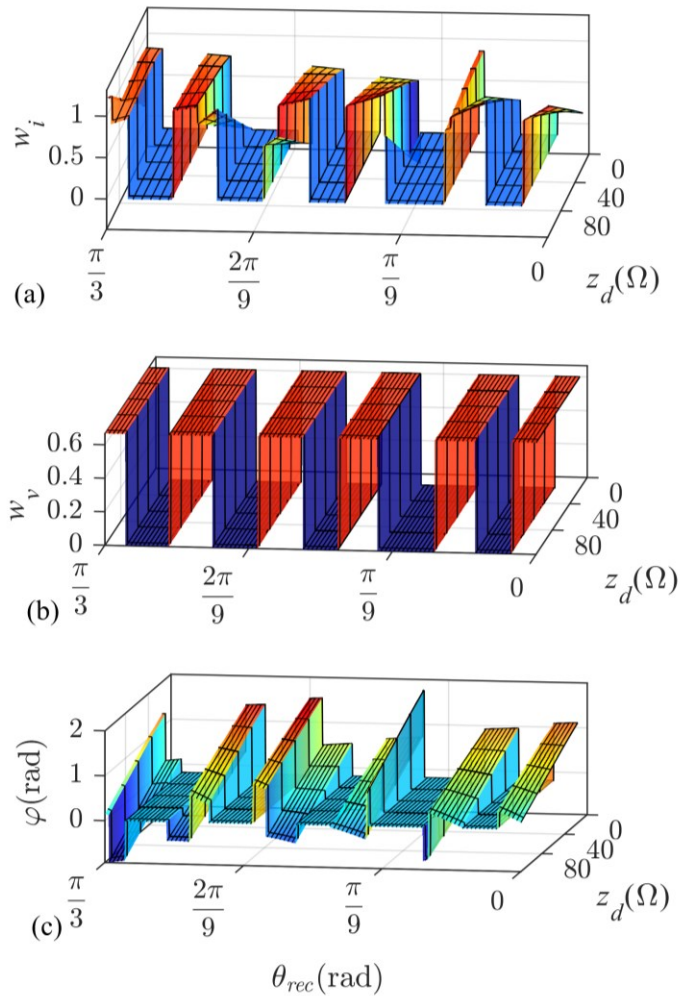
Figure 4.11 Typical parametric functions for the proposed DNSM of a VSC with for a specific modulation index M, angle δ stored in lookup tables: (a) $w_i(.)$, (b) $w_v(.)$, and (c) $\varphi(.)$.

It is noted that the construction time and size of the lookup table data are determined by the desired resolution of parametric functions and the range of operating conditions. Also, it should be noted that this is a one-time procedure and once the lookup tables are established, they can be used for various studies.

4.2   Interfacing Methods

Once the parametric functions are established as lookup tables, the proposed DNSM is readily implemented, as shown in Figure 4.12. As seen, the firing angle α (in the case of thyristor-based LCR) or modulation index M and angle δ (in the case of VSC), the source angle θ_s, the dc voltage v_{dc}, and the ac currents $\mathbf{i}_{abc}$ are the inputs to the DNSM. The ac voltages $\mathbf{v}_{abc}$ and the dc current i_{dc} are the outputs.

According to Figure 4.12, the currents $\mathbf{i}_{abc}$ coming from the external system are transformed to the qd coordinates based on (4.4). Then, z_d and θ_{rec} are computed based on (4.8) , (4.11) using the input variables v_{dc}, θ_s, and $\mathbf{i}_{qd}^s$. The values of z_d and θ_{rec} are then used along with the LCR firing angle α (or VSC modulation index M and angle δ) as the inputs to the lookup tables to compute the values of parametric functions $w_i(.)$, $w_v(.)$, and $\varphi(.)$. Afterward, the value of the output dc current is calculated based on (4.5) using $\mathbf{i}_{qd}^s$ and parametric function $w_i(.)$ as

$$i_{dc} = w_i(.)\left\|\mathbf{i}_{qd}^s\right\|. \tag{4.12}$$

54
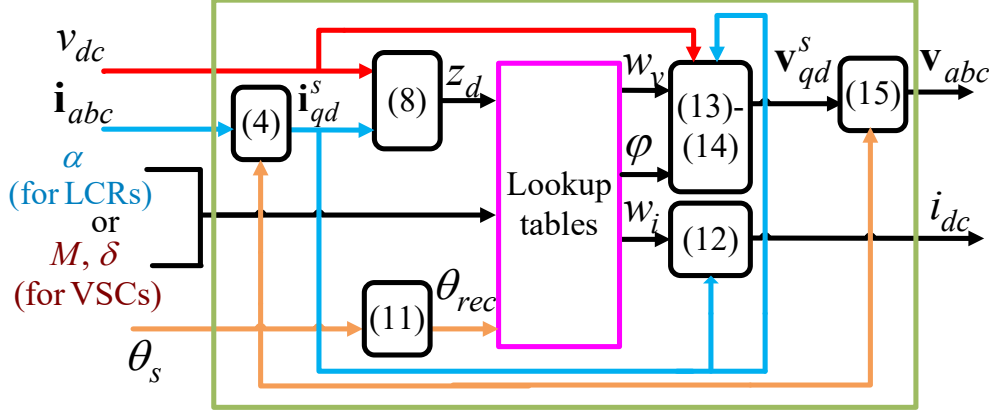
Figure 4.12 Implementation of the proposed DNSM using indirect interfacing with external networks.

Also, the converter output ac voltages in qd coordinates are calculated based on (4.6), (4.7)

using the inputs v_{dc}, $\mathbf{i}_{qd}^s$, and the computed parametric functions $w_v(.)$ and $\varphi(.)$ as

$$v_q^s = w_v(.) v_{dc} \cos\left(\tan^{-1}\left(\frac{i_d^s}{i_q^s} \right) - \varphi(.) \right), \tag{4.13}$$

$$v_d^s = w_v(.) v_{dc} \sin\left(\tan^{-1}\left(\frac{i_d^s}{i_q^s} \right) - \varphi(.) \right). \tag{4.14}$$

Finally, the *abc* voltages are computed using the inverse of Park's transformation matrix as

$$\mathbf{v}_{abc} = \left[\mathbf{K}(\theta_s) \right]^{-1} \mathbf{v}_{qd}^s. \tag{4.15}$$

4.2.1 Indirect interfacing method using controlled sources

To interface the proposed DNSM with external networks using circuit components, the

discrete switches of the converter are replaced with dependent voltage and current sources, as

depicted in Figure 4.13. Therein, the three-phase voltage sources are used to interface the output
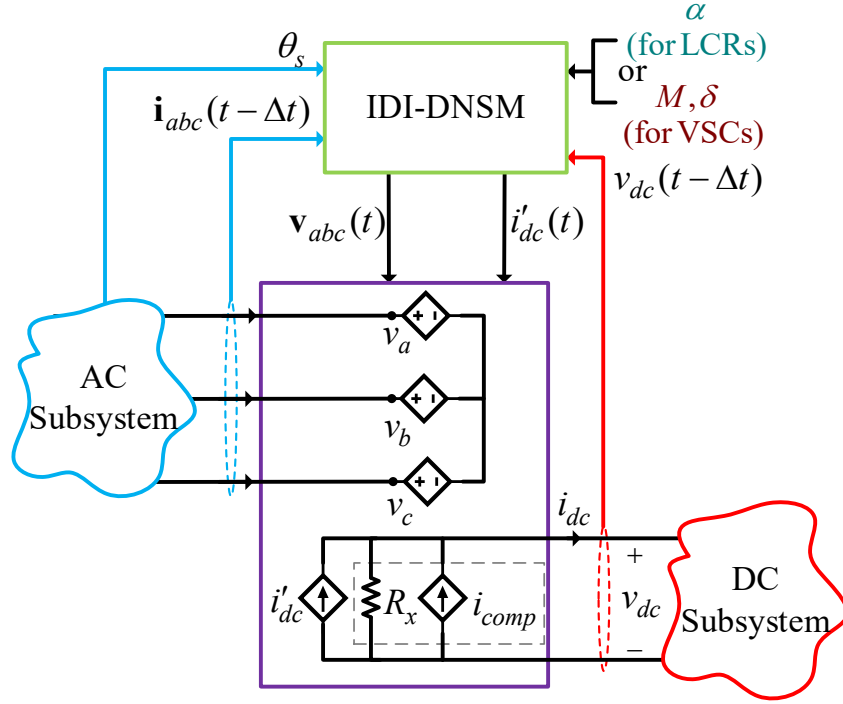
Figure 4.13 Indirect interface of the proposed DNSM with the external network using controlled current and voltage sources.

$\mathbf{v}_{abc}$ with the ac subsystem, and the controlled intermediate dc current source, calculated based on (4.12), is used to interface the output i'_{dc} with the dc subsystem.

As shown in Figure 4.13, depending on the composition of the dc subsystem, a snubber resistor R_x may be needed in parallel with the dc current source i'_{dc} when the dc subsystem cannot accept the current source at the inputs (e.g., when there is a line inductor in series with the dc current source) [59]. If a snubber is used, a compensation current source i_{comp} should be used to eliminate the steady-state error caused by the snubber current. To achieve an explicit and non-iterative interface, the compensation current i_{comp} is calculated using the input dc voltage from the previous time-step as

$$i_{comp}(t) = \frac{v_{dc}(t - \Delta t)}{R_x}.$$

(4.16)

In EMTP-type programs without an iterative solution, e.g., PSCAD and RSCAD, the inputs to the DNSM block (i.e., dc terminal voltage v_{dc} and the ac currents $\mathbf{i}_{abc}$ in Figure 4.12 and Figure 4.13) use their values from the previous time-step (i.e., $v_{dc}(t - \Delta t)$ and $\mathbf{i}_{abc}(t - \Delta t)$) since their values are not computed at the present time-step yet.

The method presented here is referred to as indirect interfacing due to using the time step delay in the interfacing variables. The interfacing delay can cause numerical inaccuracy and instability in simulations with large time steps. Therefore, the proposed indirectly-interfaced DNSM (IDI-DNSM) may not be able to run with large time-step sizes, although it still allows larger time-step sizes compared to the DSMs of converters.

4.2.2 Direct interfacing for the proposed DNSM

Inspired by [48], a direct interfacing method is developed for the proposed DNSM. The proposed directly-interfaced DNSM (DI-DNSM) is aimed to allow large time-step sizes in EMTP-type programs without the need for iterative interfacing solutions. To eliminate the one-time-step delay, the DNSM of the ac-dc converter is reformulated in the nodal solution form so that its resultant matrices and vectors can be merged with the overall network solution and solved simultaneously without a time-step delay.

The nodal equation of the overall system, including the converter, has the following general form

$$
\overset{\mathbf{G}}{} \quad \overset{\mathbf{V}}{} \quad \overset{\mathbf{I}}{}
$$

$$
\begin{bmatrix} & \vdots & \\ \cdots & \mathbf{G}_{\mathrm{CON}} & \cdots \\ & \vdots & \end{bmatrix} \begin{bmatrix} \cdots \\ \mathbf{V}_{\mathrm{CON}} \\ \cdots \end{bmatrix} = \begin{bmatrix} \cdots \\ \mathbf{I}_{h\mathrm{CON}} \\ \cdots \end{bmatrix}, \tag{4.17}
$$

where $\mathbf{V}$ is the vector of system nodal voltages, $\mathbf{G}$ is the system's conductance matrix, and the vector $\mathbf{I}$ represents the sum of injected currents to the nodes, including history currents and independent sources. Similarly, $\mathbf{G}_{\mathrm{CON}}$ is the conductance sub-matrix of the converter DNSM model, whose voltages are defined in a vector form as

$$
\mathbf{V}_{\mathrm{CON}} = [v_a(t) \quad v_b(t) \quad v_c(t) \quad v_{dc}(t)]^T. \tag{4.18}
$$

The converter currents are defined in vector form as

$$
\mathbf{I}_{\mathrm{CON}} = [i_a(t) \quad i_b(t) \quad i_c(t) \quad i_{dc}(t)]^T. \tag{4.19}
$$

The vector of history currents is defined as

$$
\mathbf{I}_{h\mathrm{CON}} = [i_{ha}(t) \quad i_{hb}(t) \quad i_{hc}(t) \quad i_{hdc}(t)]^T. \tag{4.20}
$$

First, to obtain the nodal equations for the proposed DNSM, its voltage equations are reformulated as functions of the converter currents. Then, the resultant nonlinear functions of the qd ac variables and dc variables are linearized at the time step $(t - \Delta t)$[48]. The linearized qd-dc voltages are written as

$$
\begin{bmatrix} v_q^s(t) \\ v_d^s(t) \\ v_{dc}(t) \end{bmatrix} = \begin{bmatrix} R_{qq} & R_{qd} & R_{qdc} \\ R_{dq} & R_{dd} & R_{ddc} \\ R_{dcq} & R_{dcd} & R_{dcdc} \end{bmatrix} \begin{bmatrix} i_q^s(t) \\ i_d^s(t) \\ i_{dc}(t) \end{bmatrix} + \begin{bmatrix} e_{hq}(t) \\ e_{hd}(t) \\ e_{hdc}(t) \end{bmatrix}, \tag{4.21}
$$

where

$$\begin{cases} R_{qq} = \left.\dfrac{\partial v_q^s}{\partial i_q^s}\right|_{t-\Delta t} = R_x \left(w_v(.) \left[w_i(.)\cos\left(\varphi(.)\right) + \left(\dfrac{v_{dc}}{R_x} - i_{dc}\right) \times \right.\right. \\ \qquad\qquad \left.\left. i_d^s \times \dfrac{i_d^s \cos\left(\varphi(.)\right) - i_q^s \sin\left(\varphi(.)\right)}{\left\|\mathbf{i}_{qd}^s\right\|^3} \right]\right)\Bigg|_{t-\Delta t} \\[2em] R_{qd} = \left.\dfrac{\partial v_q^s}{\partial i_d^s}\right|_{t-\Delta t} = R_x \left(w_v(.) \left[w_i(.)\sin\left(\varphi(.)\right) + \left(\dfrac{v_{dc}}{R_x} - i_{dc}\right) \times \right.\right. \\ \qquad\qquad \left.\left. i_q^s \times \dfrac{i_q^s \sin\left(\varphi(.)\right) - i_d^s \cos\left(\varphi(.)\right)}{\left\|\mathbf{i}_{qd}^s\right\|^3} \right]\right)\Bigg|_{t-\Delta t} \\[2em] R_{qdc} = \left.\dfrac{\partial v_q^s}{\partial i_{dc}}\right|_{t-\Delta t} = -R_x \left(w_v(.)\cos\left(\tan^{-1}\left(\dfrac{i_d^s}{i_q^s}\right) - \varphi(.) \right) \right)\Bigg|_{t-\Delta t} \end{cases} \tag{4.22}$$

$$\begin{cases} R_{dq} = \left.\dfrac{\partial v_d^s}{\partial i_q^s}\right|_{t-\Delta t} = R_x \left(w_v(.) \left[w_i(.)\sin\left(\varphi(.)\right) + \left(\dfrac{v_{dc}}{R_x} - i_{dc}\right) \times \right.\right. \\ \qquad\qquad \left.\left. i_d^s \times \dfrac{i_d^s \sin\left(\varphi(.)\right) + i_q^s \cos\left(\varphi(.)\right)}{\left\|\mathbf{i}_{qd}^s\right\|^3} \right]\right)\Bigg|_{t-\Delta t} \\[2em] R_{dd} = \left.\dfrac{\partial v_d^s}{\partial i_d^s}\right|_{t-\Delta t} = R_x \left(w_v(.) \left[w_i(.)\cos\left(\varphi(.)\right) + \left(\dfrac{v_{dc}}{R_x} - i_{dc}\right) \times \right.\right. \\ \qquad\qquad \left.\left. i_q^s \times \dfrac{i_q^s \cos\left(\varphi(.)\right) + i_d^s \sin\left(\varphi(.)\right)}{\left\|\mathbf{i}_{qd}^s\right\|^3} \right]\right)\Bigg|_{t-\Delta t} \\[2em] R_{ddc} = \left.\dfrac{\partial v_d^s}{\partial i_{dc}}\right|_{t-\Delta t} = -R_x \left(w_v(.)\sin\left(\tan^{-1}\left(\dfrac{i_d^s}{i_q^s}\right) - \varphi(.) \right) \right)\Bigg|_{t-\Delta t} \end{cases} \tag{4.23}$$

59

$$
\begin{cases}
R_{dcq} = \dfrac{\partial v_{dc}}{\partial i_q^s}\bigg|_{t-\Delta t} = R_x\left(\dfrac{w_v(.)i_q^s}{\left\|\mathbf{i}_{qd}^s\right\|}\right)\Bigg|_{t-\Delta t} \\[2em]
R_{dcd} = \dfrac{\partial v_{dc}}{\partial i_d^s}\bigg|_{t-\Delta t} = R_x\left(\dfrac{w_v(.)i_d^s}{\left\|\mathbf{i}_{qd}^s\right\|}\right)\Bigg|_{t-\Delta t} \\[2em]
R_{dcdc} = \dfrac{\partial v_{dc}}{\partial i_{dc}}\bigg|_{t-\Delta t} = -R_x
\end{cases}
\tag{4.24}
$$

and

$$
\begin{cases}
e_{hq}(t) = \left(v_{dc}w_v(.)\cos\left(\tan^{-1}\left(\dfrac{i_d^s}{i_q^s}\right) - \varphi(.)\right)\right)\Bigg|_{t-\Delta t} \\[2em]
e_{hd}(t) = \left(v_{dc}w_v(.)\sin\left(\tan^{-1}\left(\dfrac{i_d^s}{i_q^s}\right) - \varphi(.)\right)\right)\Bigg|_{t-\Delta t} \\[2em]
e_{hdc}(t) = v_{dc}\big|_{t-\Delta t}
\end{cases}
\tag{4.25}
$$

Then, the *qd* variables in (4.21) are transformed to the *abc* coordinates. After applying Park's

inverse transformation to the *qd* variables in (4.21), and some algebraic manipulations, the

equivalent resistance matrix of the converter DNSM in *abc* coordinates yields

$$
\mathbf{R}_{\text{CON}} =
\left[\begin{array}{ccc:c}
R_{aa} & R_{ab} & R_{ac} & R_{adc} \\
R_{ba} & R_{bb} & R_{bc} & R_{bdc} \\
R_{ca} & R_{cb} & R_{cc} & R_{cdc} \\ \hdashline
R_{dca} & R_{dcb} & R_{dcc} & R_{dcdc}
\end{array}\right] =
$$

$$
\left[\begin{array}{c:c}
\left[\mathbf{K}(\theta_s)\right]^{-1}\begin{bmatrix} R_{qq} & R_{qd} \\ R_{dq} & R_{dd} \end{bmatrix}\left[\mathbf{K}(\theta_s)\right] & \left[\mathbf{K}(\theta_s)\right]^{-1}\begin{bmatrix} R_{qdc} \\ R_{ddc} \end{bmatrix} \\ \hdashline
-\left(\begin{bmatrix} R_{dcq} & R_{dcd} \end{bmatrix}\left[\mathbf{K}(\theta_s)\right]\right) & R_{dcdc}
\end{array}\right].
\tag{4.26}
$$

Here, the positive dc current is considered outward of the converter. Therefore, a negative sign is

used with the dc-*abc* equivalent resistances to account for this convention.
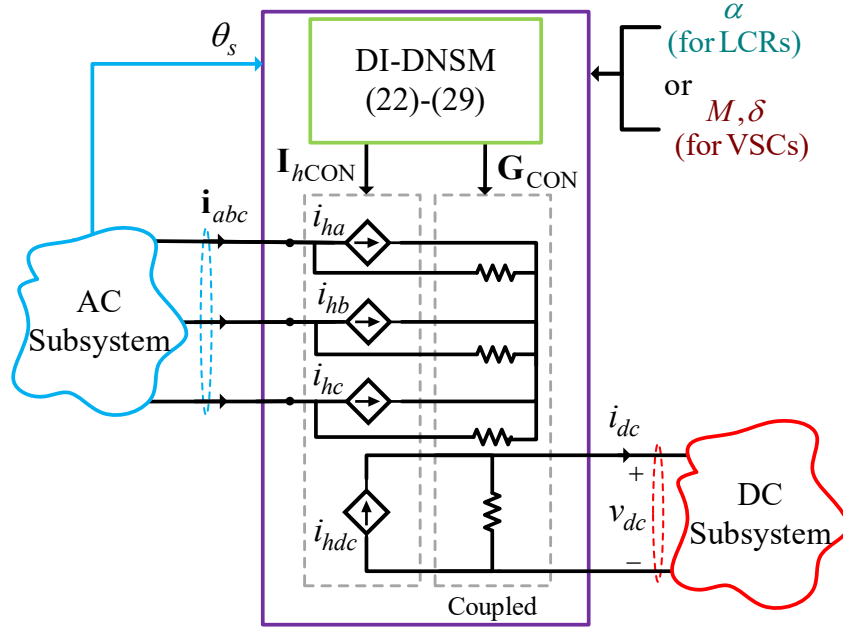
Figure 4.14 Direct interfacing of the proposed DNSM with the external network using Norton equivalent circuit.

Also, the vector of voltage history terms $\mathbf{e}_{h\text{CON}}$ in *abc* coordinates is obtained as

$$\mathbf{e}_{h\text{CON}} = \begin{bmatrix} e_{ha}(t) \\ e_{hb}(t) \\ e_{hc}(t) \\ e_{hdc}(t) \end{bmatrix} = \begin{bmatrix} \left[\mathbf{K}(\theta_s)\right]^{-1}\begin{bmatrix} e_{hq}(t) \\ e_{hd}(t) \end{bmatrix} \\ \hdashline e_{hdc}(t) \end{bmatrix}. \tag{4.27}$$

To organize the equations in the form of (4.17), the converter conductance matrix $\mathbf{G}_{\text{CON}}$ and history currents $\mathbf{I}_{h\text{CON}}$ are calculated as

$$\mathbf{G}_{\text{CON}} = \left[\mathbf{R}_{\text{CON}}\right]^{-1}, \tag{4.28}$$

and

61

$$\mathbf{I}_{h\text{CON}} = -\left[\mathbf{R}_{\text{CON}}\right]^{-1}\mathbf{e}_{h\text{CON}}. \qquad (4.29)$$

The equivalent conductance matrix $\mathbf{G}_{\text{CON}}$ calculated (4.28) and vector of current history terms $\mathbf{I}_{h\text{CON}}$ (4.29) calculated using (4.21)-(4.27), are then directly incorporated into the overall network nodal equations (4.17) when the EMT program permits. Alternatively, the proposed DI-DNSM can be interfaced using circuit components according to Figure 4.14 based on its Norton equivalent circuit.

As demonstrated in Figure 4.14, in contrast to the indirect interfacing method shown in Figure 4.13, the external snubber and compensation current are not required for the DI-DNSM as the model is already integrated into the nodal formulation. Furthermore, no input variables from the previous time step are required. This is due to the simultaneous solution of the converter's nodal equations alongside the overall network for ac and dc variables.

4.3   Computer Studies

To investigate the performance of the proposed modeling approach against the conventional detailed switching models of LCRs and VSCs, the ac–dc system in Figure 4.3 is considered with the diode- and thyristor-based LCRs, as well as VSC. The system parameters are summarized in Appendix D .

The systems with the conventional DSM of the converters have been implemented in PSCAD (offline) and RSCAD (real-time) using their standard library components. Also, the proposed DNSM is implemented in PSCAD with the indirect and direct interfacing methods, denoted as IDI-DNSM and DI-DNSM, respectively. The IDI-DNSM of the LCRs and VSCs presented in section 4.2.1 is also implemented using basic library components of PSCAD based

on Figure 4.12 and Figure 4.13. The DI-DNSM presented in section 4.2.2 is implemented as a PSCAD user-defined block by defining a conductance G matrix and a vector of history currents based on (4.26)–(4.29) and Figure 4.14. All the simulations with LCRs in PSCAD are run with disabled interpolation for the switching events for consistency with real-time simulations in RSCAD.

4.3.1   Studies with Diode-based LCR

Here, it is assumed that the LCR in Figure 4.3 consists of six diodes. The system is initially in steady-state with the LCR operating in CCM-1 mode supplying a load with $R_l = 5\,\Omega$ and $L_l = 2\,\text{mH}$. At $t = 2\,s$, the load is stepped down to $R_l = 0.5\,\Omega$, which changes the operating mode of the LCR to CCM-2. The transient response of the ac and dc variables obtained by the four subject models (i.e., DSM in PSCAD, DSM in RSCAD, and the proposed IDI- and DI-DSM in PSCAD) are shown in Figure 4.15.

The results in Figure 4.15 are obtained when the DSM in PSCAD and RSCAD are both run with a time-step of $\Delta t = 10\,\mu s$, which was the maximum possible time-step to achieve accurate results without interpolations. The two proposed IDI-DNSM and DI-DNSM are able to use much larger time steps and are run with $\Delta t = 70\,\mu s$ and $\Delta t = 200\,\mu s$, respectively.

As can be observed in Figure 4.15, the simulation results with the DSM run in offline mode (using PSCAD) and in real-time mode (using RSCAD) match almost precisely. It is also verified that the proposed IDI-DNSM and DI-DNSM are able to provide an accurate reconstruction of the entire ac and dc waveforms, consistent with the switching models, both in steady-state and in transients using much larger time steps (i.e., $70\,\mu s$ and $200\mu s$, respectively).

Figure 4.15 Transient response of diode LCR variables as obtained by the subject models for: (a) phase *a* voltage v_a, (b) phase *a* current i_a, (c) dc voltage v_{dc}, and (d) dc current i_{dc}. The DSMs in PSCAD and RSCAD are run with $\Delta t = 10 \, \mu s$, IDI-DNSM with $\Delta t = 70 \, \mu s$, and DI-DNSM with $\Delta t = 200 \, \mu s$.

Figure 4.16 depicts the waveforms of the diode LCR obtained by the conventional DSM and the proposed IDI-DNSM while both simulations are conducted in real-time using RSCAD with 70μs time-step. As can be observed, the conventional DSM is unable to accurately reproduce the ac and dc waveforms at such large time steps due to the errors in the handling of switching

64
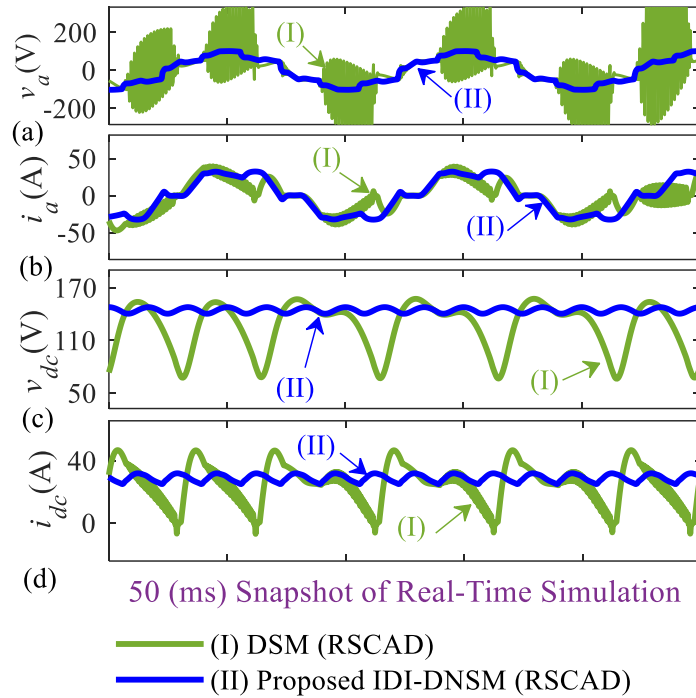
Figure 4.16 Steady-state waveforms of ac- and dc-side variables of diode LCR in CCM-1 condition as obtained by the conventional DSM and proposed IDI-DNSM run on RSCAD with $\Delta t = 70\,\mu s$: (a) phase *a* voltage v_a , (b) phase *a* current i_a , (c) dc voltage v_{dc} , and (d) dc current i_{dc} .

events; however, the proposed DNSM still achieves accurate results, similar to the waveforms in Figure 4.15. To illustrate what happens if the time step size is further increased, Figure 4.17 shows the solution of the DSM when a time step of 700 µs is used for simulation. As can be observed, the conventional DSM solution loses accuracy and becomes numerically unstable when subjected to larger time steps.
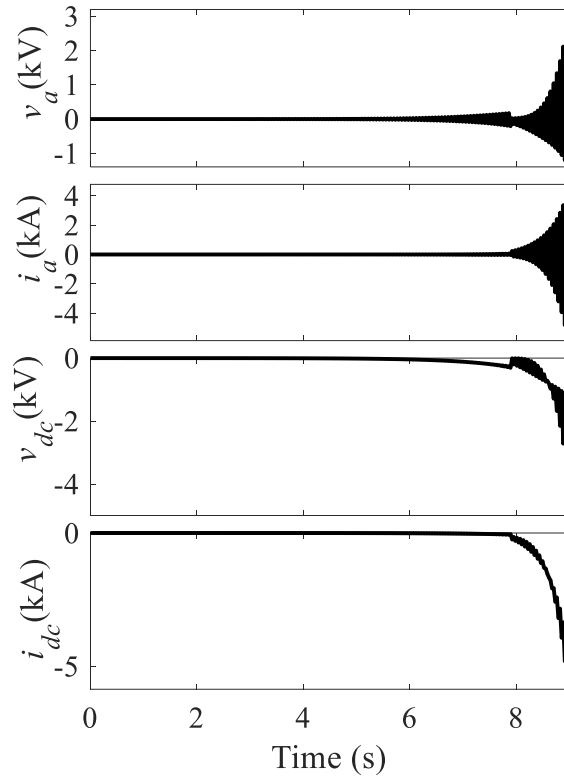
Figure 4.17 Example of unstable solution of ac- and dc-side variables of diode LCR as obtained by the conventional DSM run on PSCAD with $\Delta t = 700\,\mu s$ **: (a) phase** *a* **voltage** v_a **, (b) phase** *a* **current** i_a **, (c) dc voltage** v_{dc} **, and (d) dc current** i_{dc} **.**

4.3.2   Studies with Thyristor-LCR

Here, it is assumed that the LCR in the system of Figure 4.3 is composed of controlled thyristor switches. Initially, the system is in steady-state with the LCR operating in CCM-1 mode where the firing angle of thyristors is set to $\alpha = 35°$, and the LCR feeds a series *RL* load with
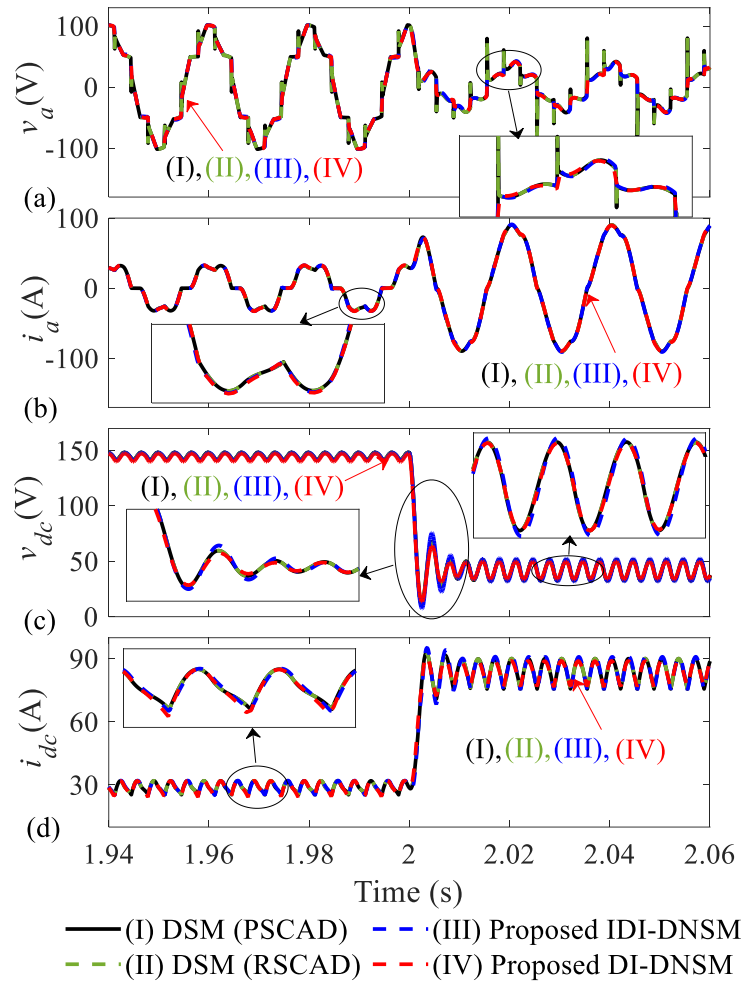
66
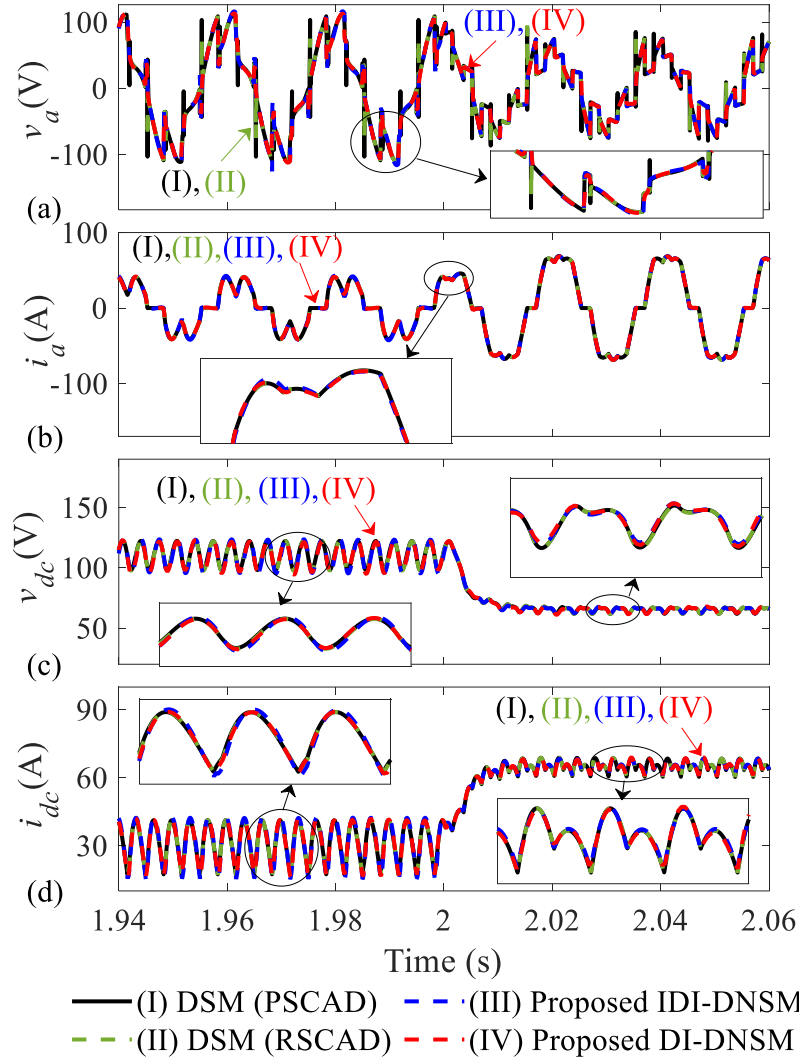
Figure 4.18 Transient response of thyristor LCR variables as obtained by the subject models for: (a) phase *a* voltage v_a, (b) phase *a* current i_a, (c) dc voltage v_{dc}, and (d) dc current i_{dc}. The DSMs in PSCAD and RSCAD are run with $\Delta t = 10\,\mu s$, IDI-DNSM with $\Delta t = 50\,\mu s$, and DI-DNSM with $\Delta t = 150\,\mu s$.

$R_l = 3.5\,\Omega$ and $L_l = 10\,\text{mH}$. Then, at $t = 2\,s$, the dc load resistance is stepped to $R_l = 1\,\Omega$ and the

firing angle steps to $\alpha = 15°$. The transient response is shown in Figure 4.18 as obtained by the

DSM in RSCAD and PSCAD (with $\Delta t = 10 \, \mu s$), the proposed IDI-DNSM (with $\Delta t = 50 \, \mu s$), and the proposed DI-DNSM (with $\Delta t = 150 \, \mu s$).

In line with the observations in Figure 4.15 for the diode-LCR, it is observed in Figure 4.18 that the results with the DSM run in offline mode (using PSCAD) and in real-time mode (using RSCAD) are consistent. It is also seen that the proposed IDI-DNSM and DI-DNSM are able to capture the entire ac and dc waveforms (including their ripples, harmonics, sharp edges, etc.) consistently with the switching models, both in steady-state and in transients. It is emphasized that the IDI-DNSM and DI-DNSM achieve this with such large time-step sizes (i.e., 50 μs and 150 μs, respectively), which is a significant numerical advantage over the DSM, which is able to run only with small time-steps (10 μs).

4.3.3   Studies with VSC

Here, the VSC in the system of Figure 4.3 is considered to have a conventional two-level topology. The switching frequency f_c is assumed to be 900 Hz using the sinusoidal pulse-width modulation (SPWM). The simulation starts from zero initial condition while the modulation index and angle are set to $M = 0.6$ and $\delta = -15°$, transferring 80 MW in steady-state from the ac subsystem to the dc subsystem. Without loss of generality, the dc subsystem here is composed of a series RL branch with $R_l = 5.99 \, \Omega$ and $L_l = 84 \, \text{mH}$, and dc voltage source $E_{dc} = 150 \, \text{kV}$, representing the inverter side of an HVDC system. Then, at $t = 1s$, the modulation index and angle are stepped to $M = 0.8$ and $\delta = -10°$, decreasing the transferred power to 70MW. Then, at $t = 2s$, the dc subsystem voltage source E_{dc} starts to fluctuate based on the profile in Figure 4.19 (a). The transient response of the system variables is depicted in Figure 4.19 (b)–(e), where the results

68
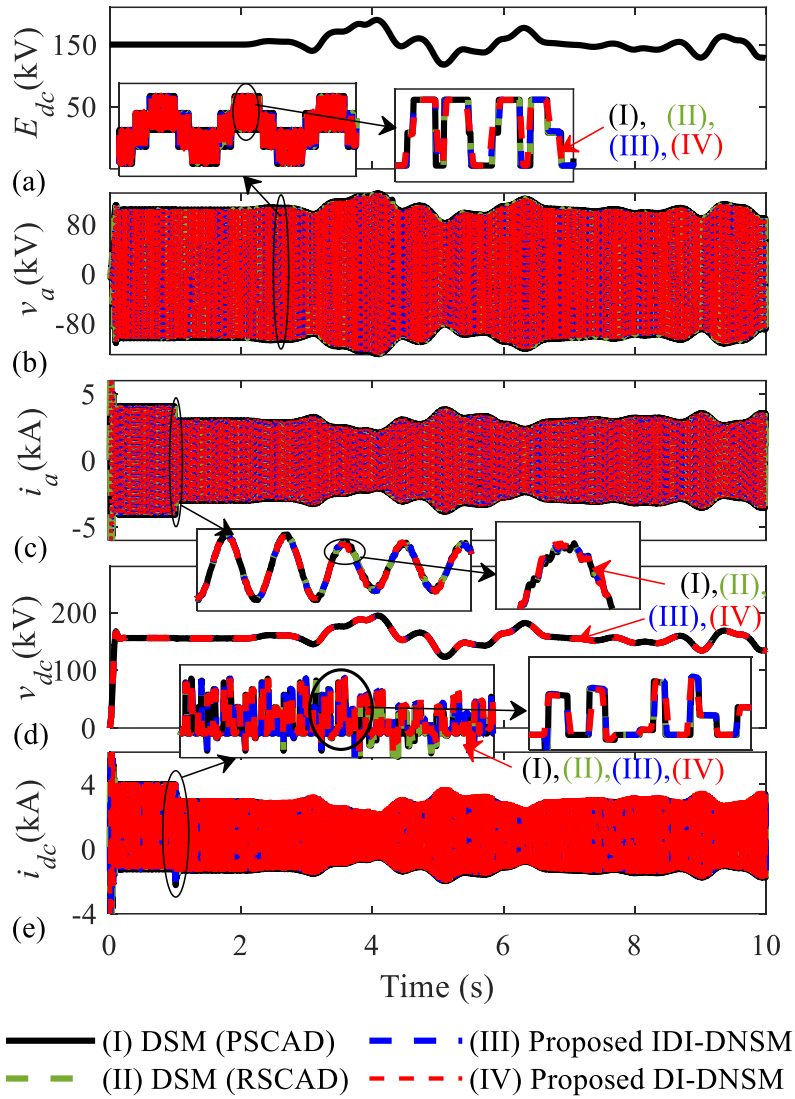
Figure 4.19 **Transient response of VSC variables as obtained by the subject models for: (a) dc subsystem voltage source E_{dc} , (b) phase *a* voltage v_a , (c) phase *a* current i_a , (d) dc voltage v_{dc} , and (e) dc current i_{dc} . The DSMs in PSCAD and RSCAD are run with $\Delta t = 10\,\mu s$, IDI-DNSM with $\Delta t = 25\,\mu s$, and DI-DNSM with $\Delta t = 50\,\mu s$.**

of the DSM in RSCAD and PSCAD are obtained with $\Delta t = 10\,\mu s$, and proposed IDI-DNSM and DI-DNSM with $\Delta t = 25\mu s$ and $\Delta t = 50\,\mu s$, respectively.

It can be observed in Figure 4.19 that the proposed IDI-DNSM and DI-DNSM accurately replicate the entire ac and dc waveforms, aligning with the DSMs. This accuracy is maintained in steady-state and transients, with larger time-step sizes of $25\ \mu s$ and $50\ \mu s$ for IDI-DNSM and DI-DNSM, respectively, achieving numerical advantages.

For the DSM of the VSC system in this paper, an accurate solution cannot be obtained without interpolation, even at very small time-steps $\Delta t < 0.01\ \mu s$, due to high-frequency switching. Therefore, the DSM of VSC in PSCAD is presented here with interpolation enabled to verify the solution provided by the proposed models. Also, the RSCAD DSM is implemented using their recently developed universal converter model (UCM) [60].

The maximum possible time-step sizes to obtain numerically valid results with the subject models are summarized in Table 4.1. As seen, the conventional DSM, IDI-DNSM, and DI-DNSM are valid up to $10\ \mu s$, $70\ \mu s$, and $200\ \mu s$ for the diode-based LCR system, respectively; $10\ \mu s$, $50\ \mu s$, and $150\ \mu s$ for the thyristor-based LCR system, respectively; and $10\ \mu s$, $25\ \mu s$, and $50\ \mu s$ for the VSC system, respectively.

4.3.4   Computational Performance Comparison

Here, the computational performance of the IDI-DNSM and DI-DNSM is benchmarked against the conventional DSM of LCR and VSC systems. The offline CPU times taken with the three subject models to run identical 30-second transient studies discussed in Sections 4.3.1, 4.3.2, and4.3.3 with different time-step sizes are summarized in Table 4.2 for the diode LCR, thyristor LCR, and VSC systems, respectively.

70

Table 4.1 Maximum possible simulation time-step with the subject models of LCR and VSC systems

Converter Model	Max Time-Step Size (µs)		
	Diode-based LCR	Thyristor-based LCR	VSC
Conventional DSM	10	10	$\Delta t < 0.01$ (Individual switch-based model)
			10 (UCM in RSCAD)
Proposed IDI-DNSM	70	50	25
Proposed DI-DNSM	200	150	50

As observed in Table 4.2, with $\Delta t = 10\,\mu s$, the proposed IDI-DNSM of diode and thyristor LCRs is computationally as expensive as the conventional DSM (taken 16.7s and 16.1s CPU time for diode LCR and 20.8s and 19.6s for thyristor LCR, respectively). In contrast, the proposed DI-DNSM requires slightly more computations (i.e., 22.3s CPU time for diode LCR and 25.1s for thyristor LCR). However, the proposed IDI-DNSM and DI-DNSM can run with larger time steps. For the diode LCR system with $\Delta t = 70\,\mu s$, they can run in 2.9s and 3.7s, respectively. Also, for the thyristor-based system at $\Delta t = 50\,\mu s$, 4.3s and 5.7s CPU times are required for IDI-DNSM and DI-DNSM, respectively. The DI-DNSM can be simulated with even larger time-steps of up to $\Delta t = 200\,\mu s$ for diode LCR and $\Delta t = 150\,\mu s$ for thyristor LCR for which only 1.4s and 2.2s is taken by the CPU, respectively.

For the VSC system, it is seen in Table 4.2 that the conventional DSM requires 58.1s CPU time with $\Delta t = 10\,\mu s$. It is noted that this time step was possible only by enabling the switching interpolation, without which the time step would have been limited to less than 0.01 μs. The proposed IDI-DNSM and DI-DNSM also have comparable performance and require 55.1s and 61.2s, respectively. The IDI-DNSM and DI-DNSM can also run faster (i.e., 24.4s and 27.3s) by

Table 4.2 Computational performance of conventional switching and proposed non-switching detailed models of diode and thyristor LCRs and VSC systems for the 30-second transient study in PSCAD

Converter	Δt (μs)	CPU Time (s)		
		DSM	Proposed IDI-DNSM	Proposed DI-DNSM
Diode-based LCR	10	16.1	16.7	22.3
	70	NA	2.9	3.7
	200	NA	NA	1.4
Thyristor-based LCR	10	19.6	20.8	25.1
	50	NA	4.3	5.7
	150	NA	NA	2.2
VSC	10	58.1	55.1	61.2
	25	NA	24.4	27.3
	50	NA	NA	15.6

increasing the time-step to $\Delta t = 25\mu s$. The proposed DI-DNSM is even able to run with

$\Delta t = 50\,\mu s$ in only 15.6s.

Chapter 5: Conclusion

The research presented in this thesis has been focused on developing numerically efficient models of ac-dc converters, including LCRs and VSCs, for their implementation in EMTP-type programs. Such converter models are considered extremely important for the practical and reliable analysis, design, and study of energy conversion power systems. Therefore, it is essential to include the harmonics and ripples of ac and dc waveforms of such converters within the model, as they significantly impact the accuracy of the results. Also, from a numerical perspective in EMTP-type programs, the converter model should possess the capability to directly interface with the program, i.e., have a simultaneous solution with the network's equations. Although several state-of-the-art models have been proposed in the literature (e.g., GPAVM, HPAVM, DI-AVMs), they either established based on indirect interfacing with the network or relied solely on average values, ignoring harmonics and ripples.

This thesis fulfills this gap in the prior state-of-the-art research by proposing a detailed continuous non-switching converter model for both indirect and direct interfacing that achieves better computational efficiency with comparable accuracy to detailed switching models. The main features and the contributions of each research objective in this thesis are summarized below.

5.1   Contributions

As part of the research presented in **Chapter 2**, the recently proposed hybrid parametric average-value detailed model (HPAVM) of the rectifier systems has been reformulated for line-commutated inverter systems. This was done by defining new dynamic admittance and parametric functions for average values and ripples/harmonics. The proposed inverter-HPAVM was used along with the rectifier-HPAVM for efficient simulation of a generic line-commutated-converter-

based classic HVDC system. It was demonstrated that the proposed HPAVM is able to reconstruct the ac and dc variables very accurately and similar to the detailed switching models of the converters while allowing much larger time steps. The application of the proposed HPAVM for converters enables superior computational performance and simulation speed (i.e., nine times faster compared to the detailed switching model) for the HVDC system, resulting in significantly reduced CPU time (10.85 seconds versus 97.7 seconds). The presented HPAVM also has the flexibility of neglecting the dc-side ripples and/or the ac-side harmonics, if desired, for more efficient simulations. It is proposed that the presented HPAVM can be an efficient asset for offline and/or real-time simulations of classic HVDC systems when large time-steps are desired.

The numerical performance of the DI-AVMs was investigated **in Chapter 3** for a hybrid LCC-VSC HVDC system implemented in PSCAD/EMTDC. Conventional implementation of average-value models (AVMs) of line-commutated converters (LCCs) and voltage-source converters (VSCs) in EMTP-type programs requires a one-time-step interfacing delay. Here, directly-interfaced AVMs (DI-AVMs) have been examined for LCCs and VSCs, which eliminate the interfacing delay. It has been verified that the conventional indirectly-interfaced AVMs lose their accuracy at time-step sizes around 100–150 μs. However, the new DI-AVMs of LCCs and VSCs can provide accurate results in simulations with very large time steps, even as large as 500 μs. This demonstrates excellent potential for DI-AVMs of LCCs and VSCs as efficient assets for real-time and offline simulations of large-scale power-electronic-based systems where utilizing large time-step sizes is desirable.

A new technique for modelling ac–dc switching converters in EMT simulators has been proposed in **Chapter 4**. The proposed technique can provide detailed waveforms consistent with the conventional switching models of converters and be used in simulations with large time steps.

This was achieved by formulating parametric functions that instantaneously relate the converter's ac and dc variables. Two interfacing methods were presented for the proposed models. With the indirect interfacing method, the proposed model was able to provide accurate results with time steps up to ~70 μs for diode and thyristor-based LCR systems, and up to ~30 μs for VSC-based systems. Meanwhile, the proposed model with direct interfacing could accurately run with time steps up to ~200 μs for LCRs, and up to ~50 μs for VSCs. It is envisioned that the proposed methodology can be beneficial for modelling switching converters in many EMT simulation programs, especially for real-time applications where achieving larger time steps with a non-iterative solution is highly desirable.

5.2   Anticipated Impact

The detailed reconstruction of converter waveforms and the adaptability of the proposed model for both direct and indirect integration within EMTP programs make the DNSM a desirable alternative. It is envisioned that the newly proposed DNSM of converters can replace the existing detailed switching converter models in commercial real-time simulators such as RTDS. The improved computational efficiency of the proposed model has the potential to expand the scope of EMT simulators to handle more extensive systems, utilizing less computational hardware resources. This advancement could lead to broader applications of EMTP programs and real-time simulators in the power industry. Consulting companies engaged in many real-time transient studies can enhance the size and level of detail in their systems due to the reduced computational cost of the proposed models compared to the traditional models.

5.3　Future Work

The research presented in this thesis will be continued in several directions. Due to limited space, only three possible paths that other students in our research group may consider are mentioned here:

The approach outlined in Chapter 2 offers detailed parametric models for line-commutated rectifiers and inverters. This approach demonstrated the capability to use larger simulation time steps compared to conventional discrete switching models. This is advantageous for conducting system-level studies of power systems containing numerous switching converters. The technique presented can be expanded to other types of power-electronic converters, including force-commutated IGBT-based converters and PWM voltage-source converters (VSCs). Additionally, it has the potential to be adapted for modelling modular multi-level converters (MMCs). It is envisioned that appropriately extending this methodology can yield AVM models for MMCs, enabling simulations with larger time steps by eliminating the requirement for zero-crossing detection.

The direct interfacing of PAVMs of LCRs is investigated in Chapter 3 for HVDC systems under symmetric and normal operating conditions. However, the failure of commutation of the converter switches may occur due to internal or external abnormal conditions, such as the fault of one or more switches, unbalanced ac sources, or faults in ac line. This requires more in-depth exploration and the appropriate formulation of the model that accurately and automatically incorporates the impact of unbalanced and asymmetric external systems on the converter operation and commutation of switches, which will have to be incorporated into the PAVM.

The converter models presented in this study for direct interfacing, including DI-AVMs and DI-DNSM, in Chapters 3 and 4, are integrated with the network's overall nodal equations

using a time-variant conductance matrix. This matrix needs to undergo computationally expensive refactorization every time step. This introduces complexity to the model and increases computational expenses. Avoiding frequent refactorization of the entire conductance matrix has been shown to enhance simulation speed. Consequently, reducing computational demands can lower CPU usage for specific studies. This strongly motivates developing converter models with constant or partially constant conductance matrices.

Bibliography

[1]   N. Mohan, T. M. Undeland, and W. P. Robbins, *Power Electronics*, 3rd ed. Hoboken, NJ, USA: Wiley, 2003.

[2]   W. Wang, A. Beddard, M. Barnes and O. Marjanovic, "Analysis of active power control for VSC–HVDC," *IEEE Trans. Power Del.*, vol. 29, no. 4, pp. 1978–1988, Aug. 2014.

[3]   T. Abedin *et al.,* "Dynamic modeling of HVDC for power system stability assessment: a review, issues, and recommendations," *Energies*, vol. 14, no. 16, pp. 4829–4854, Aug. 2021.

[4]   H. Rao et al., "Design aspects of hybrid HVDC system," *CSEE J. Power Energy Syst.*, vol. 7, no. 3, pp. 644–653, May 2021.

[5]   N. Flourentzou, V. G. Agelidis and G. D. Demetriades, "VSC-based HVDC power transmission systems: an overview," *IEEE Trans. Power Electron.*, vol. 24, no. 3, pp. 592-602, Mar. 2009.

[6]   B. He and M. Yang, "Robust LPV control of diesel auxiliary power unit for series hybrid electric vehicles," *IEEE Trans. Power Electron.*, vol. 21, no. 3, pp. 791–798, May 2006.

[7]   A. Jimenez and N. García, "Power flow modeling and analysis of voltage source converter-based plug-in electric vehicles," in *Proc. IEEE Power Energy Soc. Gen. Meet.*, 2011, pp. 1–6.

[8]   İ. Yılmaz, M. Ermiş, and I. Çadırcı, "Medium frequency induction melting furnace as a load on the power system," in *Proc. IEEE Ind. Appl. Soc. Annu. Meet.*, 2011, pp. 1–12.

[9]   S. Zhu et al., "Structure and operating performance of a double electrical excitation synchronous generator with embedded brushless synchronous exciter utilizing dc-field excitation," *IEEE Trans. Energy Convers*., vol. 37, no. 1, pp. 50–64, Mar. 2022.

[10]   J. Sottile, F. C. Trutt, A. W. Leedy, "Condition monitoring of brushless three-phase synchronous generators with stator winding or rotor circuit deterioration," *IEEE Trans. Ind. Appl.*, vol. 42, no. 5, pp. 1209–1215, Sep. 2006.

[11]   Y. Zhang and A. M. Cramer, "Numerical average-value modeling of rotating rectifiers in brushless excitation systems," *IEEE Trans. Energy Convers*., vol. 32, no. 4, pp. 1592–1601, Dec. 2017.

[12]   N. M. Haleem, A. D. Rajapakse, A. M. Gole and I. T. Fernando, "Investigation of fault ride-through capability of hybrid VSC-LCC multi-terminal HVDC transmission systems," *IEEE Trans. Power Deliv.*, vol. 34, no. 1, pp. 241–250, Feb. 2019.

[13]   H. Xiao *et al.*, "Review of hybrid HVDC systems combining line communicated converter and voltage source converter*," Int. J. Electr. Power Energy Syst*., vol. 129, no. 1, pp. 1–9 Jul. 2021.

[14]   H. Rao *et al*., "Key technologies of ultra-high voltage hybrid LCC-VSC MTDC systems," *CSEE J. Power Energy Syst.*, vol. 5, no. 3, pp. 365–373, Sep. 2019.

[15]   *Guidance Notes on Control of Harmonics in Electrical Power System*, Amer. Bureau Shipping, Houston, TX, USA, May 2006.

[16]   M. H. Bierhoff and F. W. Fuchs, "DC-link harmonics of three-phase voltage-source converters influenced by the pulsewidth-modulation strategy—an analysis," *IEEE Trans. Ind. Electron.*, vol. 55, no. 5, pp. 2085-2092, May 2008.

[17]   M. E. Villablanca, "Harmonic-free line-commutated ac/dc rectifiers," *Electr. Power Syst. Res.*, vol. 79, no. 11, pp 1531–1537, Nov. 2009.

[18]   A. M. Gole, S. Filizadeh, R.W.Menzies, and P. L.Wilson, "Optimization enabled electromagnetic transient simulation," *IEEE Trans. Power Del.*,vol. 20, no. 1, pp. 512–518, Jan. 2005.

[19]   EMTDC User's Guide v4.6, Chapter 4, Interpolation and switching. 2018. [Online]. Available: https://www.pscad.com/knowledge-base/article/163.

[20]   T. Maguire and J. Giesbrecht, "Small time-step (< 2μSec) VSC model for the real time digital simulator," in *Proc. Int, Conf. Power Syst. Transients (IPST)*, 2005, pp. 1-6.

[21]   P. M. Menghal and A. J. Laxmi, "Real time simulation: recent progress & challenges," in *Proc. Int. Conf. Power, Signals, Controls Comput.*, Jan. 2012, pp. 1-6.

[22]   M. D. Omar Faruque *et al.*, "Real-time simulation technologies for power systems design, testing, and analysis," *IEEE Power Energy Technol. Syst. J.*, vol. 2, no. 2, pp. 63-73, Jun. 2015.

[23]   Y. Huang *et al.*, "Dynamic phasor modeling of line-commutated rectifiers with harmonics using analytical and parametric approaches," *IEEE Trans. Energy Convers.*, vol. 32, no. 2, pp. 534–547, Jun. 2017.

[24]   M. Daryabak, S. Filizadeh and A. Bagheri Vandaei, "Dynamic phasor modeling of LCC-HVDC systems: unbalanced operation and commutation failure," *Can. J. Electr. Comput. Eng.*, vol. 42, no. 2, pp. 121-131, Jun. 2019.

[25]   D. Shu *et al.*, "Cosimulation of shifted-frequency/dynamic phasor and electromagnetic transient models of hybrid LCC-MMC DC grids on integrated CPU–GPUs," *IEEE Trans. Ind. Electron.*, vol. 67, no. 8, pp. 6517-6530, Aug. 2020.

[26]   P. De Rua, Ö. C. Sakinci, and J. Beerten, "Comparative study of dynamic phasor and harmonic state-space modeling for small-signal stability analysis," *Electric Power Syst. Res.*, vol. 189, 2020, Art. no. 106626.

[27]   S. D. Sudhoff, "Analysis and average-value modeling of line-commutated converter—synchronous machine systems," *IEEE Trans. Energy Convers.*, vol. 8, no. 1, pp. 92-99, Mar. 1993.

[28]   S. D. Sudhoff, "Waveform reconstruction from the average-value model of line-commutated converter-synchronous machine system," *IEEE Trans.Energy Convers.*, vol. 8, no. 3, pp. 404–410, Sep. 1993.

[29]   J. T. Alt, S. D. Sudhoff, and B. E. Ladd, "Analysis and average-value modeling of an inductorless synchronous machine load commutated converter system," *IEEE Trans. Energy Convers.*, vol. 14, no. 1, pp. 37–43, Mar. 1999.

[30]   S. D. Sudhoff, K. A. Corzine, H. J. Hegner, and D. E. Delisle, "Transient and dynamic average-value modeling of synchronous machine fed load-commutated converters," *IEEE Trans. Energy Convers.*, vol. 11, no. 3, pp. 508–514, Sep. 1996.

[31]   J. Jatskevich, S. D. Pekarek, and A. Davoudi, "Fast procedure for constructing an accurate dynamic average-value model of synchronous machine-rectifier system," *IEEE Trans. Energy Convers.*, vol. 21, no. 2, pp. 435–441, Jun. 2006.

[32]   M. Shahnazari and A.Vahedi, "Improved dynamic average value modeling of brushless excitation system in all rectification modes," *IET Elect. Power Appl.*, vol. 4, pp. 657–669, Sep. 2010.

[33]   S. Chiniforoosh *et al.*, "Definitions and applications of dynamic average models for analysis of power systems," *IEEE Trans. Power Deliv.*, vol. 25, no. 4, pp. 2655–2669, Oct. 2010.

[34]   J. Jatskevich, S. D. Pekarek and A. Davoudi, "Parametric average-value model of synchronous machine-rectifier systems," *IEEE Trans. Energy Convers.*, vol. 21, no. 1, pp. 9–18, Mar. 2006.

[35]   A. Forsyth, A. Cross, and A. Baghramian, "Approximate, average, dynamic models of uncontrolled rectifiers for aircraft applications," *IET Power Electron.*, vol. 2, no. 4, pp. 398–409, Jul. 2009.

[36]   D. C. Aliprantis, S. D. Sudhoff, and B. T. Kuhn, "A brushless exciter model incorporating multiple rectifier modes and Preisach's hysteresis theory," *IEEE Trans. Energy Convers.*, vol. 21, no. 1, pp. 136–147, Mar. 2006.

[37]   P. C. Krause, and T. A. Lipo, "Analysis and simplified representation of a rectifier-inverter induction motor drive," *IEEE Trans. Power App. Syst.,* vol. PAS-88, no. 5, pp. 588–596, May 1969.

[38]   P. Norman, J. Timothy Alt, and G. Burt, "Parametric average-value converter modeling for aerospace applications," *SAE Int. J. Aerosp.*, vol. 5, pp. 318–324, Oct. 2012.

[39]   Y. Zhang and A. M. Cramer, "Formulation of rectifier numerical average-value model for direct interface with inductive circuitry," *IEEE Trans. Energy Convers.*, vol. 34, no. 2, pp. 741–749, Jun. 2019.

[40]   H. Atighechi et al., "Dynamic average-value modeling of CIGRE HVDC benchmark system," *IEEE Trans. Power Del.,* vol. 29, no. 5, pp. 2046–2054, Oct. 2014.

[41] G. Song, T. Wang, X. Huang, and C. Zhang, "An improved averaged value model of MMC-HVDC for power system faults simulation," *Int. J. Electr. Power Energy Syst.*, vol. 110, pp. 223–231, Sep. 2019.

[42] H. Zhu, Z. Cai, H. Liu, Q. Qi, and Y. Ni, "Hybrid-model transient stability simulation using dynamic phasors based HVDC system model," *Electr. Power Syst. Res.*, vol. 76, no. 6–7, pp. 582–591, Apr. 2006.

[43] M. Daryabak *et al*., "Modeling of LCC-HVDC systems using dynamic phasors," *IEEE Trans. Power Del.*, vol. 29, no. 4, pp. 1989–1998, Aug. 2014.

[44] S. Ebrahimi, N. Amiri, H. Atighechi, Y. Huang, L. Wang, and J. Jatskevich, "Generalized parametric average-value model of line-commutated rectifiers considering AC harmonics with variable frequency operation," *IEEE Trans. Energy Convers.*, vol. 33, no. 1, pp. 341–353, Mar. 2018.

[45] S. Ebrahimi, N. Amiri, and J. Jatskevich, "Hybrid parametric average-value/detailed modeling of line-commutated rectifiers," *IEEE Trans. Energy Convers.*, vol. 35, no. 3, pp. 1494–1504, Sep. 2020.

[46] ARTEMiS CPU-based Electrical Toolbox. [online]. Available: htttps//www.opal-rt.com/resource-center/documents/resources L00161-1217.

[47] S. Ebrahimi, H. Atighechi, S. Chiniforoosh, and J. Jatskevich, "Direct interfacing of parametric average-value models of ac–dc converters for nodal analysis-based solution," *IEEE Trans. Energy Convers.*, vol. 37, no. 4, pp. 2408–2418, Dec. 2022.

[48] S. Chiniforoosh, H. Atighechi, and J. Jatskevich, "Direct interfacing of dynamic average models of line-commutated rectifier circuits in nodal analysis EMTP-type solution," *IEEE Trans Circuits Syst I Regul Pap*, vol. 61, no. 6, pp. 1892–1902, June 2014.

[49]   S. Ebrahimi and J. Jatskevich, "Average-value model for voltage-source converters with direct interfacing in EMTP-type solution," *IEEE Trans. Energy Convers.*, early access.

[50]   (2016). Simulink Dynamic System Simulation Software, User's Manual (MathWorks Inc.). [Online]. Available: http://www.mathworks.com.

[51]   Simscape Electrical (SimPowerSystems): Model and Simulate Electrical Power Systems, User's Guide, MathWorks Inc., Natick, MA, USA, 2023. [Online]. Available: http://www.mathworks.com.

[52]   (2016). *PSCAD/EMTDC*, Version. 4.2, (On-Line Help Manitoba HVDC Research Centre and RTDS Technologies Inc. Winnipeg, MB, Canada).

[53]   RTDS Simulator Software, RTDS Technologies Inc., Winnipeg, MB, Canada, 2023. [Online]. Available: http://www.rtds.com.

[54]   M. N. O. Sadiku and L. C. Agba, "A simple introduction to the transmission-line modeling," *IEEE Trans. Circuits Syst.*, vol. 37, no. 8, pp. 991–999, Aug. 1990.

[55]   S. Ma, H. Geng, G. Yang, and B. C. Pal, "Clustering-based coordinated control of large-scale wind farm for power system frequency support," *IEEE Trans. Sustain Energy.*, vol. 9, no. 4, pp. 1555–1564, Oct. 2018.

[56]   P. C. Krause, O. Wasynczuk, S. D. Sudhoff, and S. Pekarek, *Analysis of Electric Machinery and Drive Systems*, 3rd Edition, IEEE Press, Piscataway, NJ, 2013.

[57]   D. G. Holmes; T. A. Lipo, *Pulse Width Modulation for Power Converters: Principles and Practice*, 1st ed., New York, NY, USA: Wiley., 2003, pp.215-258.

[58]   N. G. Hingorani, L. Gyugyi, *Understanding FACTS: Concepts and Technology of Flexible AC Transmission Systems*, 1st ed., New York, NY, USA: Wiley., 1999, pp.67-101.

[59]   S. Ebrahimi, N. Amiri and J. Jatskevich, "Interfacing of parametric average-value models of LCR systems in fixed-time-step real-time EMT simulations," *IEEE Trans. Energy Convers.*, vol. 35, no. 4, pp. 1985-1988, Dec. 2020.

[60]   "Introducing the Universal Converter Model for enhanced real-time power electronics simulation," https://www.rtds.com/ucm.

Appendices

Appendix A : Park's Transformation Matrix and its Inverse (with neglected zero sequence)

$$\mathbf{K}(\theta_e) = \frac{2}{3} \begin{bmatrix} \cos(\theta_e) & \cos(\theta_e - 2\pi/3) & \cos(\theta_e + 2\pi/3) \\ \sin(\theta_e) & \sin(\theta_e - 2\pi/3) & \sin(\theta_e + 2\pi/3) \end{bmatrix},$$

$$\left[\mathbf{K}(\theta_e)\right]^{-1} = \begin{bmatrix} \cos(\theta_e) & \sin(\theta_e) \\ \cos(\theta_e - 2\pi/3) & \sin(\theta_e - 2\pi/3) \\ \cos(\theta_e + 2\pi/3) & \sin(\theta_e + 2\pi/3) \end{bmatrix}.$$

Appendix B : Parameters for the Case Study of Subsection 2.2

Parameters of the AC Subsystems

$$\mathbf{e}_{abc}^{rec} = 228.4 \text{ kV}, \qquad \mathbf{e}_{abc}^{inv} = 199.8 \text{ kV}, \qquad f_e^{rec} = f_e^{inv} = 60 \text{ Hz},$$

$$r_s^{rec} = r_s^{inv} = 1 \ \Omega, \qquad L_s^{rec} = L_s^{inv} = 10.01 \text{ mH}.$$

Parameters of the DC Subsystem

$$r_l = 2.5 \ \Omega, \qquad L_l = 596.8 \text{ mH}, \qquad C_l = 26 \ \mu\text{F}.$$

Appendix C : Parameters for the Case Study of Subsection 3.2

Parameters of AC Subsystems:

$\mathbf{e}_{abc,1} = 188$ kV, $\qquad \mathbf{e}_{abc,2} = 132$kV, $\qquad f_{s,1} = f_{s,2} = 60$ Hz, $\qquad r_{s,1} = r_{s,2} = 1\ \Omega$,

$L_{s,1} = r_{s,2} = 0.037$ H.

Parameters of DC Subsystem:

$r_{line} = 2.5\ \Omega,\ \ L_{line} = 0.5968$ H,

$C_{line} = 26\ \mu\text{F},\ \ \ C_{dc} = 500\ \mu\text{F}, \qquad R_x^{\text{LCR}} = R_x^{\text{VSC}} = 150\Omega$

Appendix D : Parameters for the Case Study of Subsection 4.3

LCR system parameters:

$E_{rms} = 90\,\text{V}, \; f_s = 50\,\text{Hz}, \; r_s = 1\Omega, \; L_s = 1\,m\text{H}, \; C_f = 500\,\mu\text{F}, \; R_x = 100\Omega,$

$R_{on\_switch} = 0.091\Omega, \; V_{on\_switch} = 0.637\,\text{V}.$

VSC system parameters:

$E_{rms} = 70.7\,k\text{V}, \; f_s = 60\,\text{Hz}, \; f_c = 900\text{Hz}, \; r_s = 1.5\Omega,$

$L_s = 37.14\,m\text{H}, \; C_f = 3000\,\mu\text{F}, R_x = 150\Omega.$